UNIVERSITY OF OKLAHOMA

GRADUATE COLLEGE

RAPID ELEMENTAL ANALYSIS USING X-RAY FLUORESCENCE AND LASER INDUCED BREAKDOWN SPECTROSCOPY, AND THEIR APPLICATIONS IN THE MISSISSIPPIAN MERAMEC, ANADARKO BASIN, OKLAHOMA

A THESIS

SUBMITTED TO THE GRADUATE FACULTY

In partial fulfillment of the requirements for the

Degree of

MASTER OF SCIENCE

By

HEYLEEM HAN

Norman, Oklahoma

2020

RAPID ELEMENTAL ANALYSIS USING X-RAY FLUORESCENCE AND LASER INDUCED BREAKDOWN SPECTROSCOPY AND THEIR APPLICATIONS IN THE MISSISSIPPIAN MERAMEC, ANADARKO BASIN, OKLAHOMA

A THESIS APPROVED FOR THE

MEWBOURNE SCHOOL OF PETROLEUM AND GEOLOGICAL ENGINEERING

BY THE COMMITTEE CONSISTING OF

Dr. Carl Sondergeld

Dr. Chandra Rai

Dr. Deepak Devegowda

Acknowledgements

I would like to thank Dr. Carl Sondergeld and Dr. Chandra Rai for their mentorship, support, patience, and knowledge throughout the course of my thesis. I would like to thank Dr. Deepak Devegowda, Dr. Ali Tinni, and Dr. Mark Curtis for their input and support. I would like to thank Dr. Richard Larese for sharing his point count petrographic analysis and his guidance.

I thank the Oklahoma Geological Survey for access to its core facility (OPIC) especially to Ms. Vyetta Jordan, Mr. Jeffery S. Dillon and Mr. Scott A. Bryant for providing access to the cores used in this study and the members of Integrated Core Characterization Center especially Micaela J. Langevin, Gary D. Stowe, and Jeremy Jernigen for helping us perform the measurements. Mr. Bruce Spears for automating the XRF acquisition. Also, I thank the members of the Unconventional Shale Gas Consortium and our Marathon Oil Corporation-OU JIP (Chris McLain and James Packwood) for their support and guidance. I also thank Integrated Core Characterization Center for their support.

I would like to thank Dr. Son Dang for his support, patience, and knowledge throughout the extent of the project. I would like to thank all of my friends in IC^3 for their support and encouragement. Lastly, I would like to thank my family for their love and support.

Table of Contents

List of tables

List of figures

Abstract

X-Ray fluorescence (XRF) and Laser Induced Breakdown spectroscopy (LIBS) are rapid elemental analysis techniques for rock cores and cuttings. Elemental analysis is useful in understanding geochemical, mineralogical, diagenetic and petrophysical characteristics of rock formations. Specific elemental concentrations, or their ratios, can be used as proxies to understand sedimentary depositional environments, diagenetic overprints, and organics. High spatial resolution XRF and LIBS data acquisition allow the capture of high frequency spatial changes in rock formations, providing a more accurate decision input for the target zones in horizontal drilling. Also, elemental analysis on cuttings across multiple wells can help geoscientists build a more robust reservoir model. The application of these scanning techniques reduces analysis time and quickens decision making.

Elemental analysis on eight cores of the Mississippian Meramec in STACK (Sooner Trend Anadarko basin Canadian and Kingfisher counties) play was conducted using XRF and LIBS instruments. High resolution mineralogy profiles were generated from elemental data using internal inversion software which showed a trend with clay increasing and calcite decreasing in the depositional direction (NW to SE). From this elemental mineralogy database, both geological and petrophysical information were extracted.

A model to predict high resolution porosity profiles was built using XRF elemental and mineralogy data. Brittleness is a formation property used in completion decisions. Mineralogy composites from elemental data were used to calculate a brittleness index. Furthermore, I attempted to identify the zones with biogenic quartz using Si and Zr proxies.

During the Mississippian period, most of the study area was covered by carbonate systems, and carbonate diagenesis was observed throughout the core. By integrating point count petrographic analysis with XRF data, quantification of carbonate diagenesis using Sr-ratio (Sr/(Ca+Mg)) was conducted. In the depositional direction, an increase of Sr-ratio implies that the formation suffered less carbonate diagenesis. High spatial resolution XRF data can capture formation heterogeneity. By comparing the 2 inch spatial resolution profile and 2 foot resolution profiles derived from smoothing XRF data, quantification of the degree of heterogeneity across the wells was performed. In the depositional direction, the formation became less heterogeneous as less discrepancy between the two rescaled data sets is observed. Lastly, in the distal direction, total organic carbon (TOC) concentration from LIBS as well as GRs and clay index were observed to increase.

Chapter 1: Introduction

1.1. Rapid elemental scanning tools

Elements in sedimentary rocks have been used as proxies to understand marine or terrestrial sedimentary histories and depositional environments (Weissert et al., 2008). Elemental analysis of materials can be done with many tools, such as coupled plasma atomic emission spectroscopy and mass spectrometry (ICP-OES-MS) and benchtop glass fused X-ray fluorescence (XRF). These techniques are known to be precise and accurate, but they require significant time and sample preparation. Handheld XRF, on the other hand, is comparatively fast, non-destructive, easy to use and requires little or no sample preparation. The recently developed handheld LIBS can be complementary to XRF, since it can measure light elements such as carbon (both organic and inorganic) and sodium, which XRF cannot.

1.1.1 X-ray fluorescence

XRF has been successfully used in laboratory settings to determine the elemental composition of samples for geochemical, industrial, and archaeological applications for decades (e.g. Hevesy, 1932; Shaw, 1952; Parrish, 1956; Norrish and Hutton, 1969; Norrish and Chappell, 1977; Jenkins et al., 1995; Jenkins, 1999; Beckhoff et al.,2006).

Handheld/portable XRF was developed for various industries by several different manufacturers, including Brucker, ThermoScientific, and OLYMPUS. As a result, it was possible to acquire compositional information in the field in a real-time in many industries, such as mining, meteoritics, geochemistry (e.g. Potts et al., 1995; Shrivastava et al., 2005; Markey et al., 2008; Potts and West, 2008; Phillips and Speakman, 2009; Liritzis and Zacharias, 2010; Zurfluh et al., 2011; Young et al., 2016)

XRF measurements usually show a significantly higher signal-to-noise ratio and more consistent core-to-core correlation than other physical property measurements, such as density or color reflectance (Croudace and Rothwell, 2015). Therefore, it provided extensive archives for time-series analysis of relatively complete sections (e.g. e.g. Pälike et al., 2001; Jaccard et al., 2005; Tjallingii et al., 2007).

1.1.2 Laser Induced Breakdown spectroscopy

As LIBS has capacity to detect multi-elements, has a fast response time, and requires little or no sample preparation; it has been used in diverse fields such as food, manufacturing plants, and space missions on Mars for elemental analysis (Deguchi and Wang., 2016). Earliest applications of LIBS date from the 1980s (e.g. Cremers and Radziemski, 1983; Cremers et al., 1984). Over the past three decades, LIBS has been applied to geological materials, mostly focused on quantitative determination of a few elements (e.g. Grant et al., 1991; Bolger, 2000; Hilbk-Kortenbruck et al., 2001; Bustamante et al., 2001; Harmon et al., 2006; Gottfried et al., 2009). It has recently started being used in the petroleum industry for shale characterization (e.g. Washburn, 2015; Xu et al., 2015; Sanghapi et al., 2016; Han et al., 2019; Jain et al., 2019).

Washburn (2015) showed application of LIBS to predict organic geochemistry and mineralogy using 145 shale samples. Geochemistry parameters including TOC, S1, S2, S3, Tmax etc. LECO® TOC and programmed pyrolysis were used as reference measurements. For the mineralogy comparison, XRD was used as a reference measurement.

Sanghapi et al. (2016) reported quantitative analysis of 7 elements including silicon, aluminum, titanium, magnesium, calcium, arsenic, and carbon using ten outcrop samples from the Marcellus shale (eight samples were used for the calibration and two samples were used for the validation set). ICP-OES and carbon analyzer were used for reference measurements. These measurements

show a strong correlation between LIBS predictions and reference measurements, but a larger sample size should be measured to validate these findings.

Jain et al., 2019 constructed elemental 2D maps and reported quantification analysis for 7 elements (hydrogen, carbon, iron, magnesium, silicon, aluminum, and calcium) on Marcellus and Bakken samples. ICP-OES and a LECO CHN TureSpec™ analyzer were used for reference measurements. The number of samples used was not reported.

1.2 Chemostratigraphy

Geochemical proxies have been used to interpret formations and understand depositional environments. “Chemostratigraphy started in the early 1980s, but the basic concept of chemostratigraphy has matured as much as stratigraphy itself” (Ramkumar, 2015).

For the study of conventional reservoirs, the principles of chemostratigraphy have been used for correlations in complex settings, identifying sediment origin, and determining depositional cyclicity (e.g. Ratcliffe et al., 2004; Pearce et al., 2005; Svendsen et al., 2007; Pe-Piper et al., 2008; Hildred et al., 2010; Ratcliffe et al., 2010).

For the study of unconventional reservoirs, chemostratigraphy was extensively adopted in many areas, such as identifying shale source rocks, determining organic carbon presence, determining the redox state near the sediment/water interface, determining mineralogy, and identifying brittleness zones (e.g., Algeo and Maynard, 2004; Turgen and Brumsack, 2006; Tribovillard et al., 2008; Wright et al., 2010; Jenkyns, 2010; Ratcliffe et al., 2012a,b; Altamar and Marfurt, 2014; Driskill et al., 2018).

Conventionally, geoscientists use similarity of well log responses to develop mudrock correlations. However, stratigraphic correlations can be ambiguous, providing multiple possible cases as

depicted in **Fig. 1** (Treanton, 2014; Turner, 2016). There are three possible facies shifts in this case, and the best way to verify the correlation is to collect additional data. Elemental proxies acquired from rapid scanning tools (XRF and LIBS) can be useful to construct sequence-stratigraphic framework (Turner, 2016; Coronado, 2018).

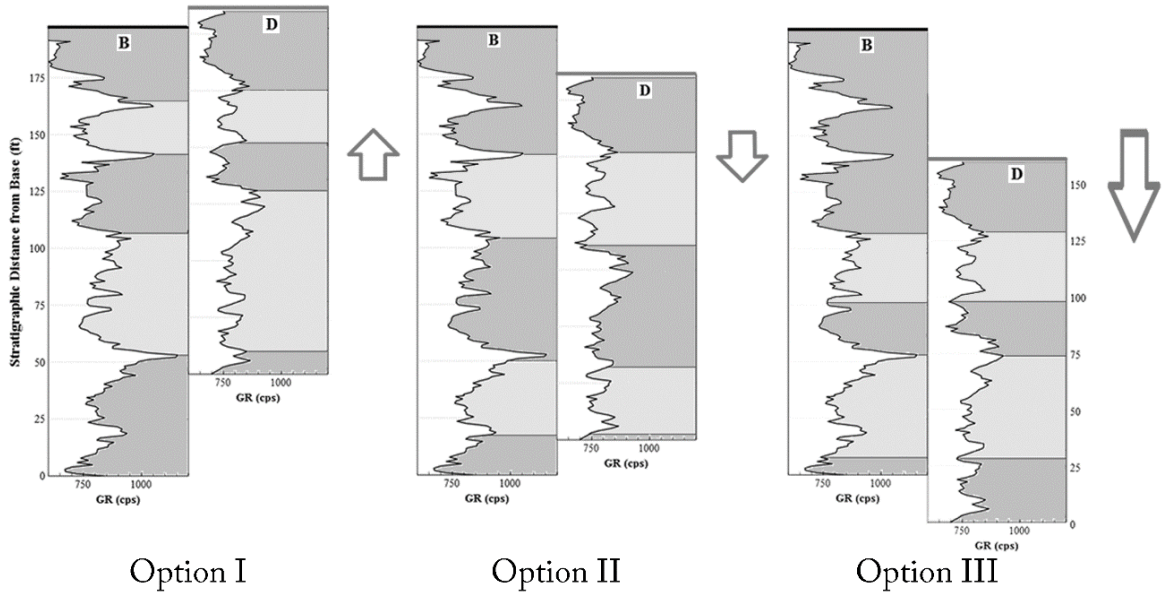

Figure 1: Gamma ray correlations of samples from Hunton Anticline Quarry. B and D are a quarter mile apart. It shows three possible correlations from option I to option III. Additional data such as elemental proxies can help find the right shift for these multiple ambiguous correlations. Image was acquired from Treanton 2014) and Turner (2016).

Major and trace elements have been used as indicators of climate and environmental transitions at the time of sediment accumulation (Aldahan et al., 2000, Weissert et al., 2008). Major elements are used to invert for mineralogy such as quartz, carbonates, feldspar, and clays in rock formation. Silicon is associated with detrital quartz, clays, feldspars, and biogenic quartz (Pearce and Jarvis, 1992; Pearce et al., 1999; Sageman and Lyons, 2004). Aluminum and potassium are associated with clays and feldspars (Pearce et al., 1999; Tribovillard et al., 2006; Turner, 2016). The ratio of silicon to aluminum (Si/Al) is associated with quartz proxy including both detrital and biogenic quartz (Pearce and Jarvis, 1992; Pearce et al., 1999; Sageman and Lyons, 2004; Turner, 2016). On

the other hand, the ratio of aluminum to silicon (Al/Si) is related to fine silt and clays (Van-Daele et al., 2014; Clift et al., 2014)

Calcium is associated with carbonate sources (Banner 1995; Tribovillard et al., 2006) and magnesium is related to detrital dolomite (Lauterbach et al., 2011). Strontium is also a proxy for carbonate sources (Banner 1995; Tribovillard et al., 2006; Driskill et al., 2018). Most carbonates are susceptible to mineralogical change, cementation, and dissolution. Carbonate diagenesis happens when it comes in contact with water and is greatest near the sediment surface and during shallow burial. In marine settings, carbonate diagenesis can take place near the sediment surface where fresh waters penetrate the sediments, affecting porosity (Bathurst, 1971; Milliman, 1974; Scholle, 1978; Longman, 1980; Choquette and Pray, 1970). Strontium with calcium and magnesium can be used for diagenetic movement of elements during the event of carbonate cements (Tucker and Wright, 1990; Edgar et al., 2015; Driskill et al., 2018).

Titanium and zirconium are associated with continentally derived sediment (Sagemand and Lyons, 2004; Bhatia and Crook 1986; Turner, 2016). Therefore, the relationship between Zr and Si has been used to differentiate between detrital quartz and biogenic quartz: a positive correlation between Zr and Si can represent detrital quartz trend and negative correlation can represent biogenic quartz trend (Wright et al., 2010; Ratcliffe et al., 2012b; Driskill et al., 2018).

A standard requirement for TOC preservation is a reducing environment. In oxygen-deficient environments, trace metals are enriched because of their lower solubility. Therefore, redox-sensitive elements have been used as a proxy for TOC. Those elements include molybdenum, vanadium, nickel, uranium, copper, zinc, and chromium (Tribovillard et al., 2006; Driskill et al.,

2018; Hart et al., 2019). Turner et al. (2016) compared the Mo concentration to TOC concentration in Woodford shale samples and interpreted the Mo-TOC signals with regard to sea level change. Driskill et al. (2018) showed comparisons between TOC concentration and seven redox sensitive elements using samples from Bone Spring and Wolfcamp formations, and three elements (nickel, copper, selenium) showed a good match with TOC concentration.

1.3 Study area

Elemental analysis using handheld XRF and LIBS was conducted on eight cores of the Mississippian Meramec. The study wells are located in Sooner Trend Anadarko basin Canadian and Kingfisher counties (STACK) plays of the Oklahoma's Anadarko basin. **Fig. 2** shows the paleogeographic map of the late Mississippian period. The red box indicates a superposition of the current location of Oklahoma and the star represents the area where the wells are located. As delineated in **Fig. 2**, during Mississippian period, most of the area was an extensive carbonate system with low gradient depositional slope (Frazier and Schwimmer, 1987; Price et., 2020).

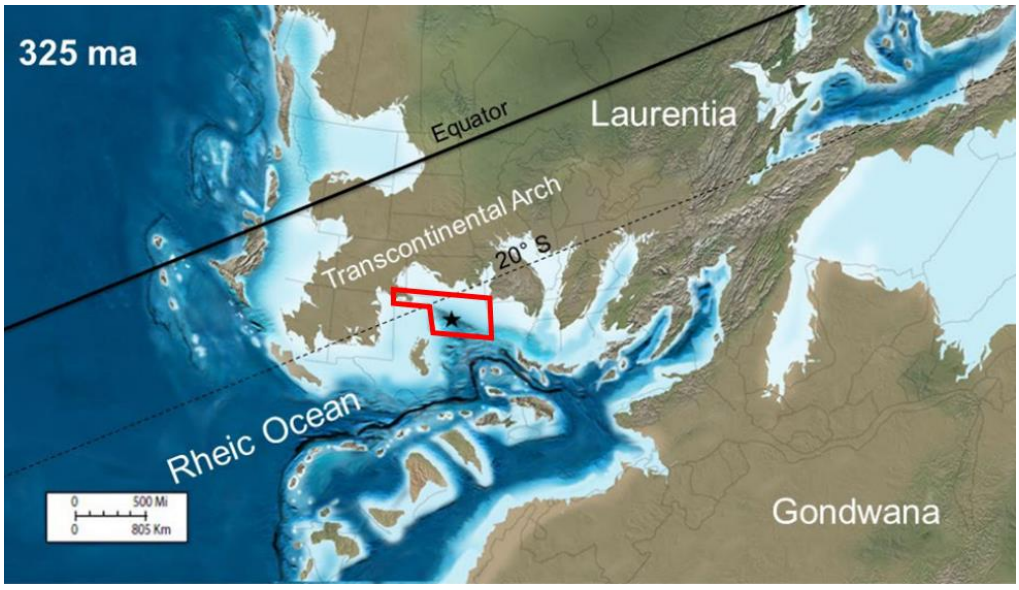

Figure 2: Paleogeographic map of the late Mississippian period. Red box represents a superposition of the current location of Oklahoma and the star indicates the area of the wells studied. This figure is modified from the map compiled by Blakey (2014).

Fig. 3 shows the schematic depositional model of the study area. Proximal shallow-water conditions were present to the north, and the water level deepens towards the south into the basin (Lane, 1978; Lane and De Kyser, 1980; Gutschick and Sandberg, 1983). The play was deposited with gradual changes, from higher-energy, more calcareous facies updip to lower energy argillaceous facies basin ward (Coronado, 2018; Miller, 2019; Hardisty, 2019; Price et al., 2020). During the Mississippian period, the direction of paleowind was likely from northeast to southwest (Witzke, 1990). Preferential wind direction possibly drove longshore currents, which redistributed sediment brought from updip (Price et al., 2020). Price et al. (2020) also pointed out that the primary driver of reservoir quality is the quantity of calcite cement, which is largely found in coarser-grained, higher energy facies, whereas porosity is preserved in lower-energy facies.

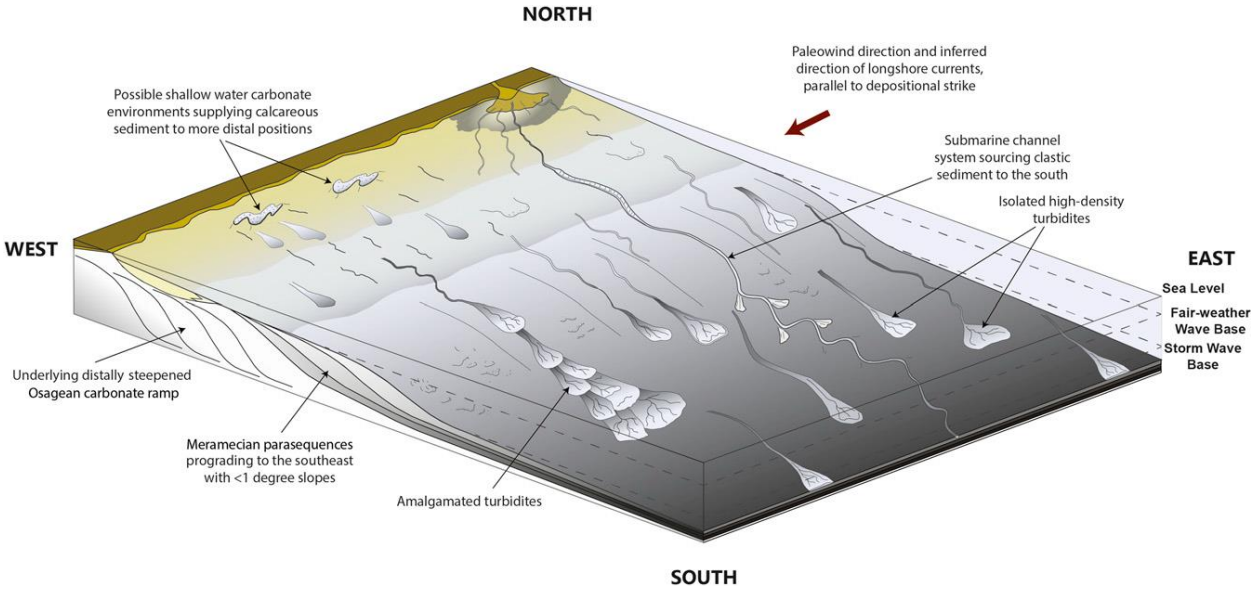

Figure 3: Schematic depositional model. Figure was acquired from Price et al. (2020). The system is composed of a series of low angle parasequences stepping from the northwest to the southeast. During the Mississippian, the direction of paleowind was likely from northeast to southwest (Witzke, 1990). Preferential wind direction possibly drove longshore currents that redistributed sediment brought from updip (Price et al., 2020).

Fig 4. shows the locations of wells where core samples were acquired for elemental analysis in the STACK play. This map is expanded from the black star area depicted in **Fig. 2**. Eight cored wells were scanned using XRF and LIBS and **Table 1** shows the information of each well, including depth range and resolution of measurements. In total, 16,162 XRF measurements and 2,421 LIBS measurements were taken. The grey arrow in **Fig. 4** indicates the depositional direction (NW to SE). Sections 3.1 to 3.6 will discuss the results from the XRF data taken from the cross section from well A to well G depicted in **Fig. 4-a**. Section 3.7 will discuss the results from LIBS elemental data taken from the cross section from well H to well G depicted in **Fig.4-b**.

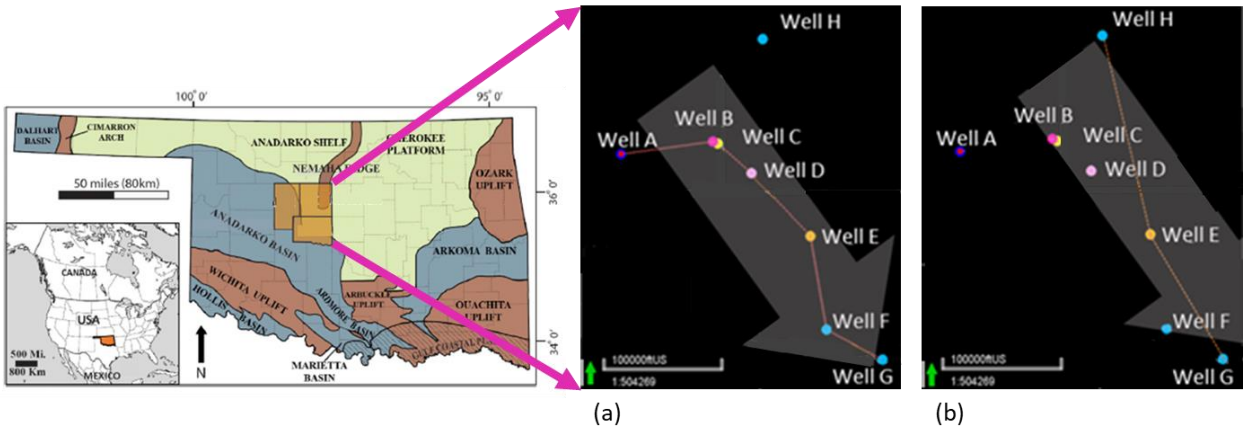

Figure 4: Map of wells of study area located in STACK plays, Anadarko basin, Oklahoma, which is expanded from the black star from Fig. 2. Grey arrow indicates the depositional direction (northwest to southeast). (a) shows the direction from well A to well G. Section 3.1 to 3.6 will show the results of elemental analysis following (a) direction using XRF elemental data. Section 3.7 will discuss about the results following (b) direction. Figure on the left hand side is modified from Northcutt and Campbell, 1996.

Table 1: List of eight core scanned by XRF and LIBS. Depth range and resolution of each measurement are shown. In total, 16,162 XRF measurements and 2,421 LIBS measurements were acquired on cores and plugs. Since LIBS calibration for carbon estimation was accomplished later, carbon concentration was acquired from only well E, G, and H.

Measurement		XRF		LIBS		
Well	Depth range, ft	Resolution, inch	The number of data	Resolution, ft	The number of data	Available of carbon estimation
Well A	XX340 ~ XX786	2	2,360, 81*	4	73*	X
Well B	X654 ~ X890	2	870, 20*	1	240	X
Well C	X708 ~ X923	2	930, 16*	1	150	X
Well D	X416 ~ X890	1	4,330, 267*	4	120*	X
Well E	X095 ~ X610	1	4,150, 91*	0.5	1008	O
Well F	X848 ~ XX221	2	1,880, 27*	1	400	X
Well G	X895 ~ X964	2	270	0.5	110	O
Well H	X746~X920	2	870	0.5	320	O
Total number of data		-	16,162	-	2,421	-

* samples measured on plug samples.

The Meramec is composed of seven stratigraphic zones (Hardisty, 2019). **Fig. 5-a** shows relative sea level change with sequence stratigraphy of Meramec from Price et al. (2017). Price et al. (2017) stated that Meramec deposition shows increasing cyclicity over time. **Fig. 5-b** shows the GR response of one well, which shows an increasing cyclicity trend.

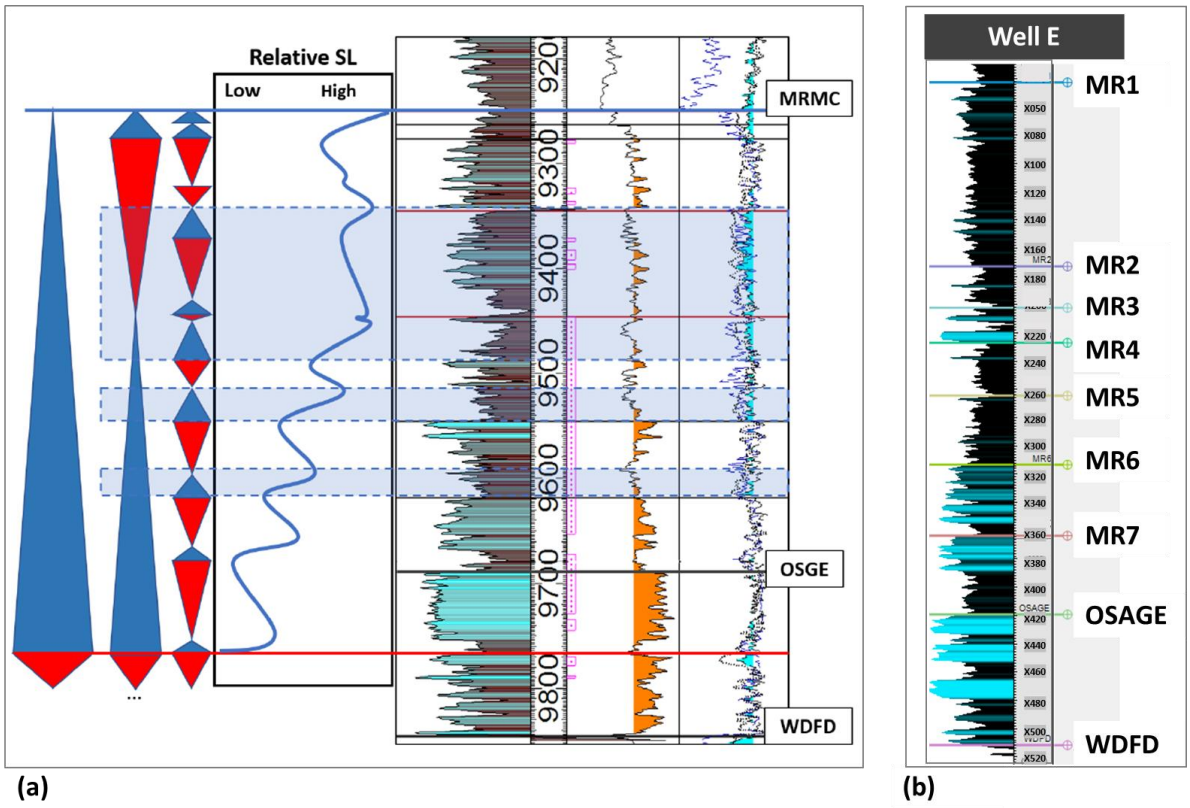

Figure 5: (a) Relative sea level curve and sequence stratigraphy of Meramec from Price et al. (2017). It shows increasing cyclicity. (b) GR response and zonation of well E. Increasing cyclicity can be seen during Meramec deposition as well. The zones marked MR define the total Meramec sequence which is composed of seven stratigraphic zones.

1.4 Synopsis

This thesis contains four chapters. Chapter 1 gives the introduction of rapid elemental scanning tools: handheld X-ray fluorescence (XRF) and Laser Induced Breakdown spectroscopy (LIBS). They are applied to cores from 8 different wells from the Mississippian Meramec in STACK (Sooner Trend Anadarko basin Canadian and Kingfisher counties) plays of the Oklahoma's Anadarko basin. This will introduce the geological setting of the study area. Chapter 2 discusses principles of XRF and LIBS and their inversion results for elemental quantification. It also presents the workflow to acquire total organic carbon (TOC). Chapter 3 describes the results of elemental

analysis applied to eight cores from the study area along with discussions of the results. Chapter 4 provides conclusions and recommendations from this study.

Chapter 2: Methods

2.1 X-ray Fluorescence (XRF)

Measurements were taken with handheld XRF instrument (TRACER 5i™ by BRUKER), a portable analyzer based on energy dispersive X-ray fluorescence technology; it uses an X-ray tube as the excitation source (6-50kV) and can analyze magnesium to uranium; 27 elements under air conditions.

2.1.1 Principle of XRF

XRF is a rapid and nondestructive method of elemental analysis; **Fig. 6** is an illustration of how it works. Primary X-rays bombard electrons on the surface of a material, primarily inner-shell electrons of atoms, and result in vacancies. In order to maintain the stability, electrons from outer-shells fill the vacancies, releasing the excess energy in the form of X-ray fluorescence radiation. This radiation is used to characterize the elements in the material by the XRF instrument's detector; the intensity of the radiation is proportional to the concentration of the elements detected (Pollard et al., 2007; Perrone et al., 2014). **Fig. 7** shows an example of a spectrum acquired. The x-axis shows energy in keV (kiloelectron volts) and y-axis shows intensity in cps (counts per second). Each element has characteristic peaks at specific energy levels depending on K, L, and M lines. (a) shows all the peaks of elements, and (b) shows the peaks of major elements present in the sample. The table in **Fig. 7** shows the actual elemental concentrations of the spectrum from XRF inversion. The concentrations of trace elements are denoted as ppm units.

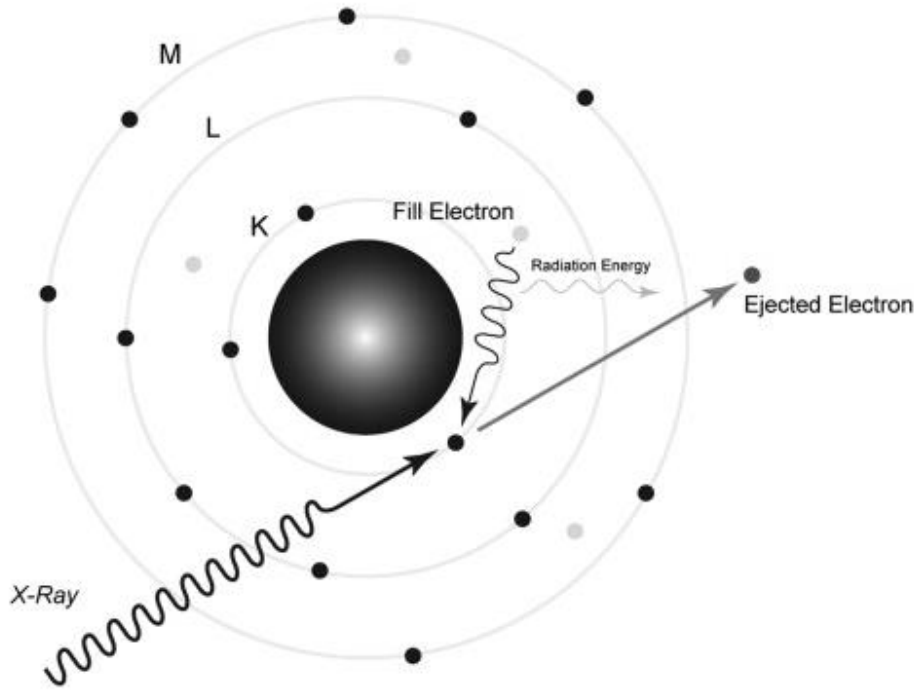

Figure 6: Illustration of how XRF works. X-rays (primary) bombard individual electrons primarily inner-shell electrons of atoms and result in vacancies. In order to restore the stability, electrons from an outer-shells fill the vacancies releasing the excess energy in the form of X-ray fluorescence radiation (secondary) which is characteristic of elements (from Perrone et al., 2014)

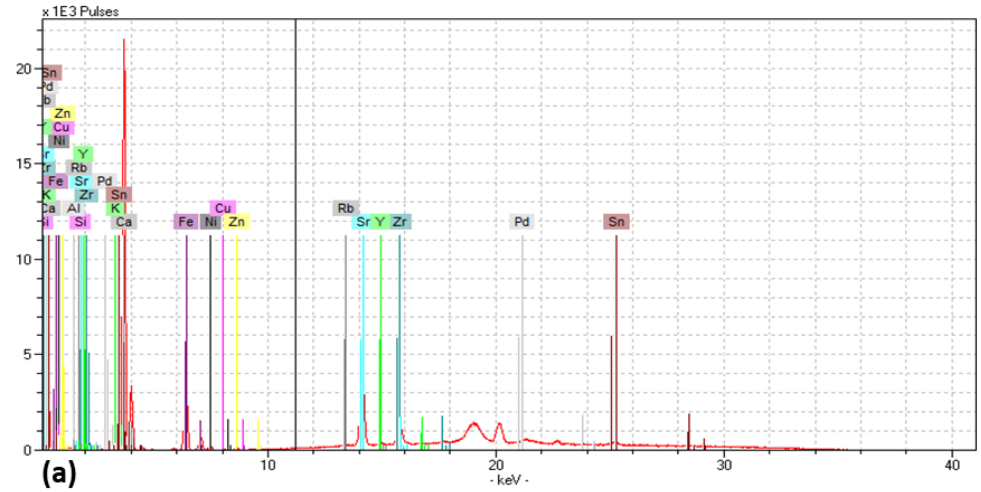

Element	wt %
Ca	23.2
Si	8.0
Mg	1.1
Fe	1.0
Al	0.8
S	0.2
K	0.2

Element	ppm
Ti	1080.8
Sr	956.0
Zr	130.0
Mn	111.0
Ni	48.9
Cr	36.4
Zn	36.2

Element	ppm
Y	21.9
Rb	17.2
U	6.4
Mo	4.4
Nb	3.4
Co	2.7
Pb	2.0

Element	ppm
Th	1.3
P	0.0
Cu	0.0
As	0.0
Ba	0.0
V	0.0

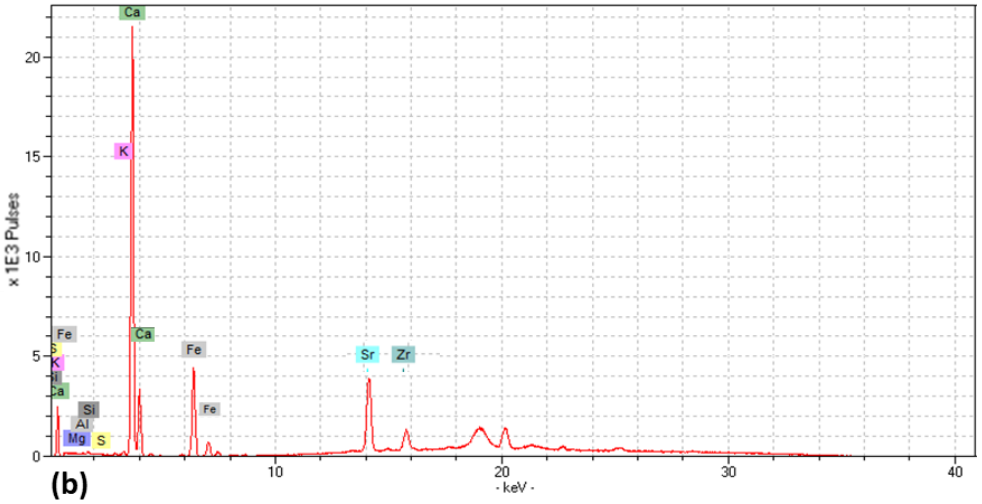

Figure 7: An example of an XRF spectrum. X-axis shows energy in keV (kiloelectron volts) and y-axis shows intensity in cps (counts per second). Each element has characteristic peaks at specific energy level depending on K, L, and M lines. (a) shows all elemental peaks, and (b) shows the peaks of major elements present in the sample. The table shows the actual elemental concentrations based on the inversion of the XRF spectrum. The concentrations of trace elements are denoted as ppm units.

Even though portable XRF has many advantages, it has limitations in that it cannot detect light elements such as carbon and sodium due to the attenuation particularly when coupled through air.

Fig. 8 shows XRF response. The incident X-ray beam in blue penetrates the sample, exciting electrons. The emitted energies in red are recorded by the detector. **Equation 1** shows the Beer-Lambert Law which includes an attenuation coefficient, path length, and element concentration. Intensity of transmitted light and path length is closely related to molecular weight because heavier elements will emit X-rays with relatively high fluorescent energy that are less susceptible to absorption with deeper response depths. In other words, light elements have low energy and can only be transmitted through relatively small response depths. Also, measurements in air with a protective film layer on the beam window will significantly intensify light element attenuation effect (Potts, 1987; Jenkins, 1988; and Croudace and Rothwell, 2015).

$$A = -log(\frac{I_x}{I_0}) = \varepsilon bc \qquad \text{Eq. 1}$$

Where,

A = absorbance

I_x = intensity of transmitted light

I_0 = intensity of incident light

ε = molar attenuation coefficient, $L*cm^{-1}mol^{-1}$

b = path length of the beam of light through the material sample, cm

c = concentration, $mol*L^{-1}$

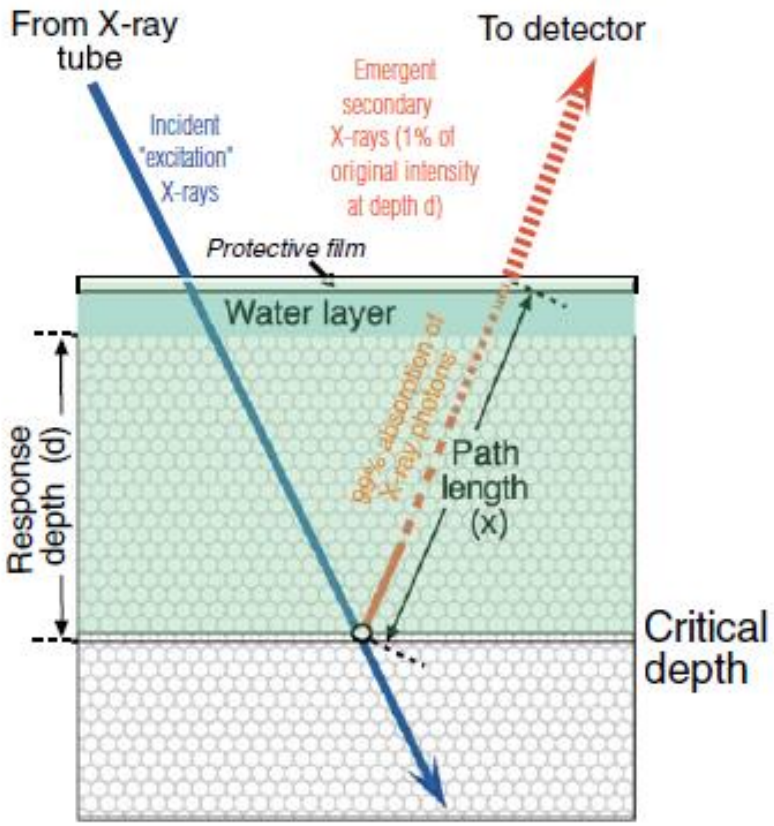

Figure 8: Illustration of XRF response. The incident X-ray beam in blue penetrates the sample exciting electrons and the emitted energies in red are recorded by the detector. The green area indicates the volume from which the signal comes from. Lighter elements are more susceptible on attenuation effect with relatively small response depths than heavier elements (after Craudace and Rothwell, 2015).

2.1.2 IC^3 XRF automated scanning system

The handheld XRF unit used at the IC^3 is mounted on an automated scanning system. It is user independent, minimizes human errors, and can maintain the standoff distance between the instrument and the core. **Fig. 9** is an image of the apparatus running on the core in an automatic system. It can move in both the x-axis and y-axis and can run 9 ft of slabbed core per batch. It takes 75 seconds per measurement under the 'Mudrock' Dual calibration setting, and about 2.5 hours to finish running the 9 ft section at a 1 inch sampling interval.

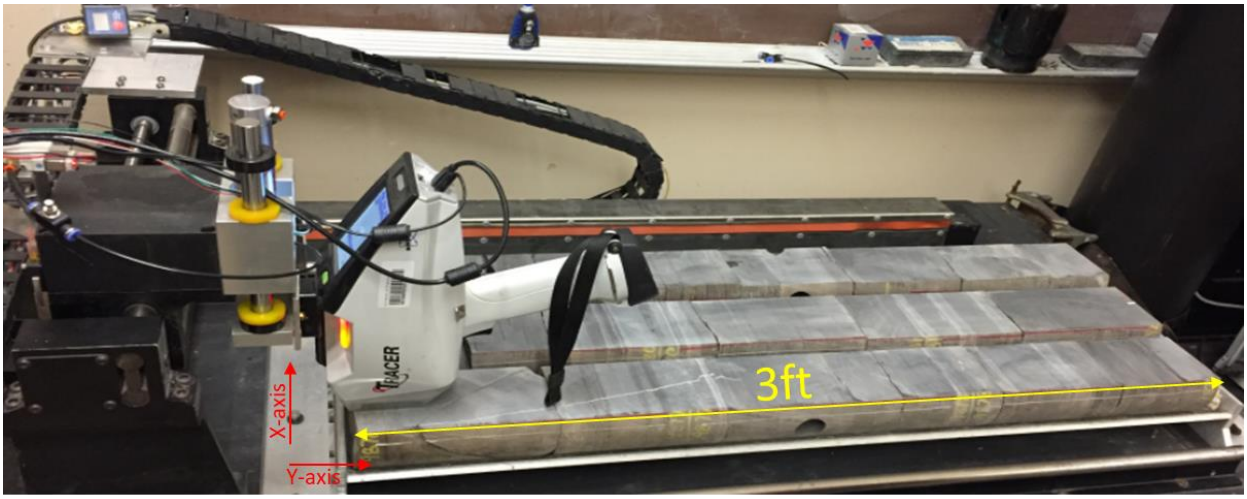

Figure 9: IC^3 XRF automated scanning apparatus shown with three, 3-foot slabbed sections of core ready to be scanned. The user sets an interval down to a minimum of 0.1" and can define exceptions for missing core or gaps in the core.

2.1.3 Inversion results

IC^3 XRF has Mudrock Dual calibration on the system which allows detection of both major and trace elements. In order to check the calibration, internal standards were made using 16 major minerals: calcite, quartz, dolomite, albite, kaolinite, illite, orthoclase, sodium montmorillonite, calcium montmorillonite, siderite, aragonite, chlorite, attapulgite, biotite, muscovite, and pyrite. As for standards preparation, pure minerals were ground and mixed in different concentrations, then pressed into pellets (32mm diameter, 4mm thickness). 50 such pellets were prepared and analyzed using XRF. Pure minerals were sent out to a commercial company for ICP OES-MS testing. **Fig. 10** shows the comparison between XRF and ICP measurements; results are in weight percentage. The elements show a strong correlation with the exception of sulfur. Sulfur showed a slope of 1.45, and sulfur concentration was adjusted based on the coefficient.

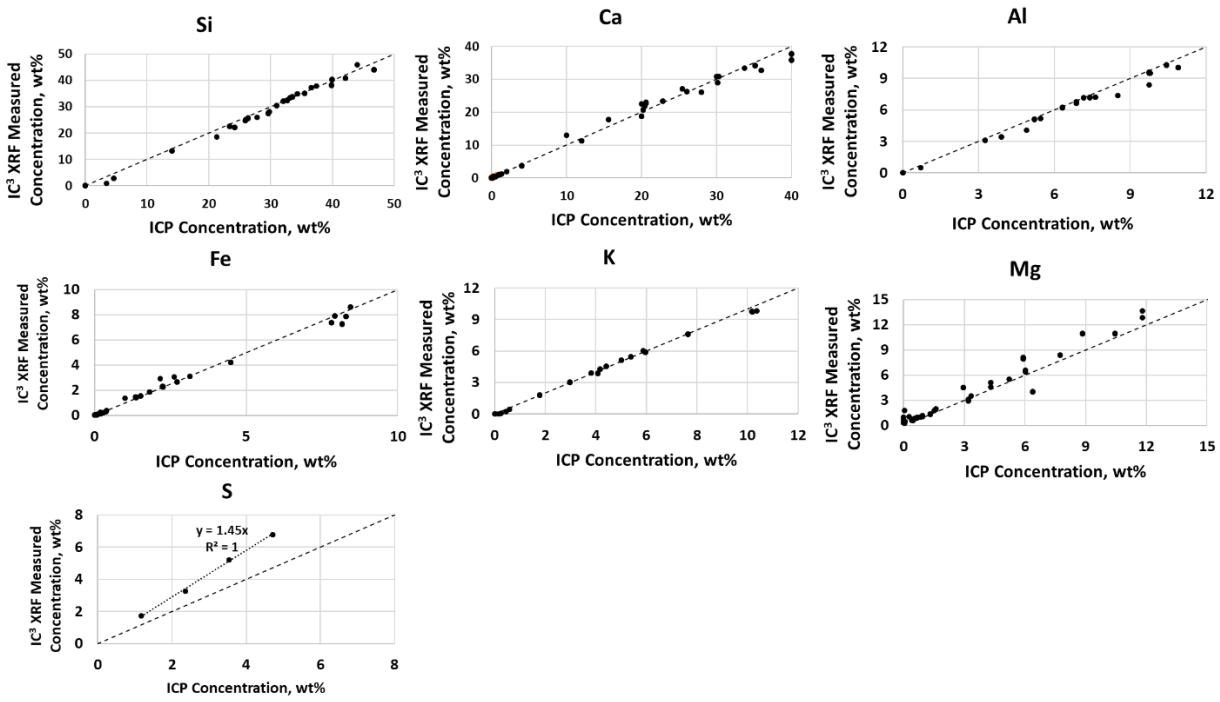

Figure 10: Comparison between XRF and ICP measurements. X-axis shows the ICP concentration in weight % and y-axis shows XRF concentration in weight %. They agree well each other following the 1:1 line except for sulfur. Sulfur showed the slope 1.45 and it this coefficient was used to adjust the concentration of sulfur.

2.2 Laser Induced Breakdown spectroscopy (LIBS)

LIBS is a type of atomic emission spectroscopy that uses laser pulses as an excitation source. A Z-300® handheld instrument from SciAps was used. The spectrometer of the instrument covers a wavelength range of 190 nm to 950 nm, which detects almost every element from hydrogen to uranium, except for sulfur and cesium.

2.2.1 Principle of LIBS

Fig. 11 shows the instrument image on the left and an illustration of how LIBS works on the right. A pulsed, high-energy laser is focused on a sample, generating plasma plume that contains the sample's excited atoms and ions. As the plasma cools, the atoms and ions return to a stable state

and emit light of specific wavelengths. An on-board spectrometer analyzes the emitted light by measuring the wavelength and intensity.

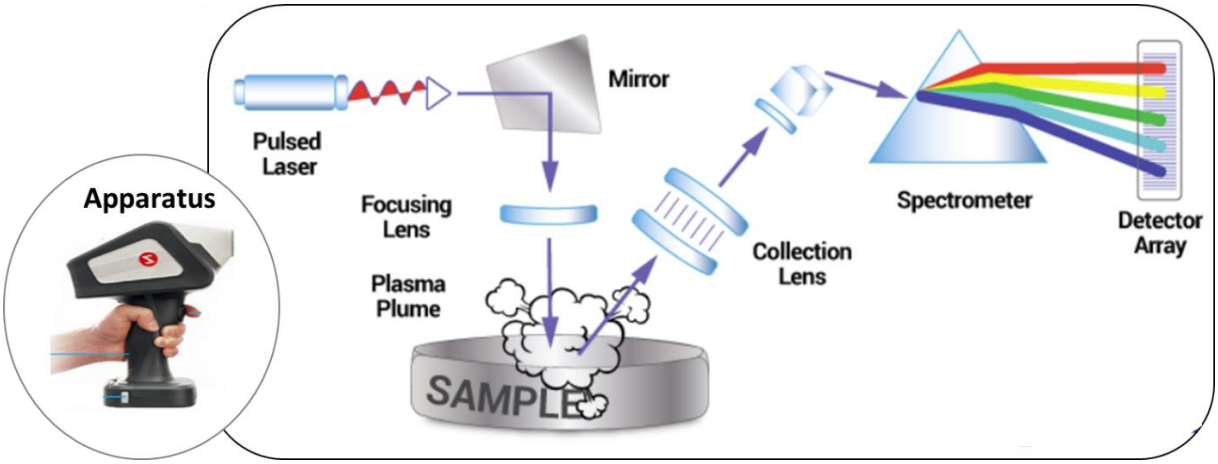

Figure 11: An image on the left shows Z-300® handheld instrument used. An illustration on the right shows how LIBS works. Pulsed laser is focused on the sample producing plasma plume. As the plasma cools, excited atoms and ions return to their ground states emitting light. An on-board spectrometer analyzes the emitted light by measuring the wavelength and intensity (Images acquired from SciAps webpage at 4/20/2020).

Fig. 12 shows an example of spectrum acquired from a LIBS instrument. It shows intensity of light emission on the y-axis as a function of wavelength on the x-axis. It detects the wavelength ranging from 190 nm to 950 nm which covers a partial ultraviolet (UV), full visible light, and a partial infrared (IR). Each element has distinctive emission signals at specific wavelengths. For example, carbon has two major emission lines at 195 nm and 248 nm.

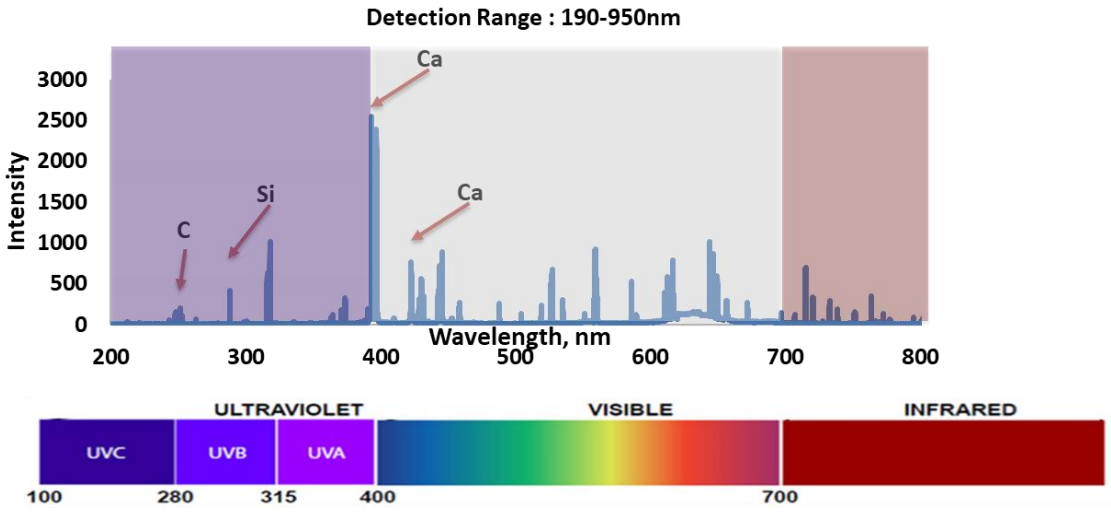

Figure 12: An example of spectrum acquired from LIBS instrument. Y-axis is the intensity of light and x-axis is wavelength ranging from 190 nm to 950 nm which covers a partial ultraviolet (UV), full visible light, and a partial infrared (IR). Each element has distinctive emission lines at specific wavelengths. For example, carbon has two major emission line at 195 and 248 nm.

The signal to noise ratio was enhanced by using an argon purge during measurement, which eliminated atmospheric contamination (Effenberger et al., 2010). Wavelength calibration was conducted every hour to maintain spectral consistency. **Fig. 13** shows an example of an SEM image of an array of laser ablation spots on the surface of a shale sample. In order to minimize the heterogeneous nature of the samples, 12 laser ablation spots are shot at each sample depth (each spot size is about 100μm in diameter), which together cover an area of about 1 mm^2. At each ablation point, laser ablation was performed 13 times, including 3 cleaning shots to remove surface contamination and 10 spectra acquisition shots. Therefore, the final LIBS spectra acquired for a sample is the average from 120 individual data shots and it only takes about 10 seconds to acquire a final spectrum.

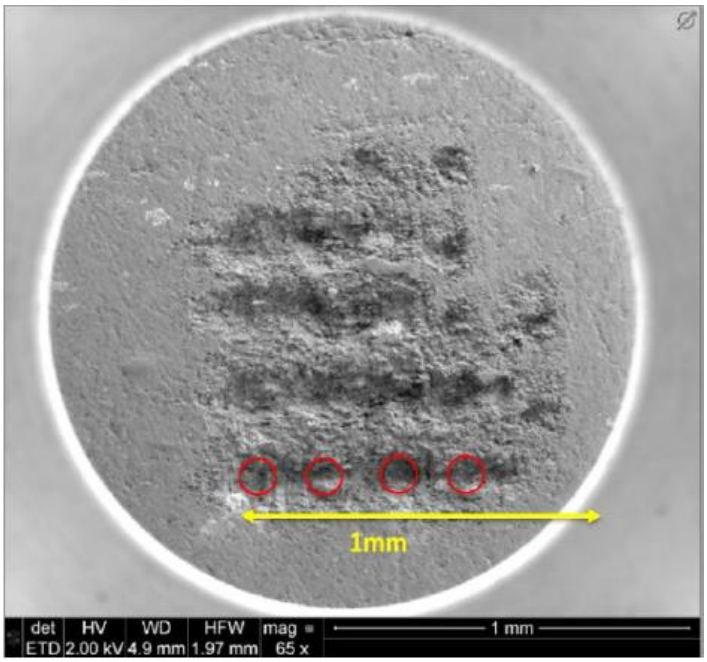

Figure 13 : SEM image of laser ablation spots on the surface of a sample. 12 laser ablation spots (4x3 rater pattern) are shot for each sample (each spot size is about 100 µm in diameter), which together cover of about 1 mm^2 area. Red circles indicate each ablation spot. At each ablation point, laser ablation was performed 13 times, including 3 cleaning shots to remove surface contamination and 10 spectra acquisition shots. The final LIBS spectra acquired for a sample is the average from 120 individual data shots and it only takes about 10 seconds to acquire a final spectrum.

2.2.2 Sample selection and spectra acquisition to build an inversion.

In order to convert qualitative spectral data into quantitative elemental concentrations, an inversion method was developed using 150 rock samples. **Table 2** shows the list of samples from 7 different tight shale formations: Woodford, Eagle Ford, Wolfcamp, Meramec, Bakken, Marcellus, and Vaca Muerta. These 150 samples were used as a training set to build an inversion program, and a separate group of 100 samples were used as a validation set. XRF and LECO® measurements were used to calibrate the LIBS spectra. XRF was calibrated with ICP-OES-MS measurements on the standard samples (see **Fig. 10)**. The LECO® data was acquired without acidizing the samples, and provided total carbon, both organic and inorganic. **Table 3** shows dynamic ranges for each

elemental concentration within the training dataset and measurement methods used for the calibration of each element. For carbon estimation, LECO without acidization was used. For the rest of the elements (silicon, calcium, aluminum, potassium, iron, magnesium) XRF was used.

Table 2: The list of samples used for LIBS inversion. 150 samples from 7 different tight shale formations were used as a training set to build an inversion. 100 samples were used as a validation set.

	Formation	The number of samples
Training set	Woodford	9
	Eagle Ford	23
	Wolfcamp	20
	Meramec	77
	Bakken	6
	Marcellus	7
	Vaca Muerta	5
	Total	**150**
Validation set	Woodford	45
	Wolfcamp	10
	Meramec	27
	Bakken	13
	Marcellus	5
	Total	**100**

Table 3: Dynamic ranges for each elemental concentration within the training dataset and measurement method used for the calibration for each element. For the carbon estimation, LECO without acidization was used which provides total carbon including inorganic and organic carbon. For the rest of elements such as silicon, calcium, aluminum, potassium, iron, and magnesium, XRF measurements were used.

Element	Si	Ca	Al	K	Fe	Mg	Total C
Range, w%	0-42	0-41	0-9	0-4	0-5	0-10	0-19
Calibration method	XRF (previously ICP calibrated)						LECO ® without acidization

Each element has emission lines at specific wavelengths, so it is important to collect good spectra from each sample for accurate inversions. Because of the attenuation (Croudace and Rothwell, 2015), as the integrated delay time increases, intensity of spectral peaks decreases. **Fig. 14-a** shows examples of two different emission lines: one at 393.3 nm, and the other at 259.9 nm. Intensity on the y-axis is exponentially attenuated as a function of integrated delay time on the x-axis. The decay trends vary for different emission lines and decay coefficients were acquired based on each curve. **Fig. 14-b** shows how the decay coefficients change as a function of wavelength. The x-axis shows the emission line in ***nm*** and the y-axis shows decay coefficient. Decay coefficient decreases as the wavelength of emission line increases. This is especially important in the case of carbon. Carbon's major emission lines are at short wavelengths (192-245 nm), so the attenuation effect becomes greater. Therefore, it is critical to determine the optimal integrated delay time while acquiring LIBS spectra from organic rich samples. Optimal integrated delay time was set as 5 ns.

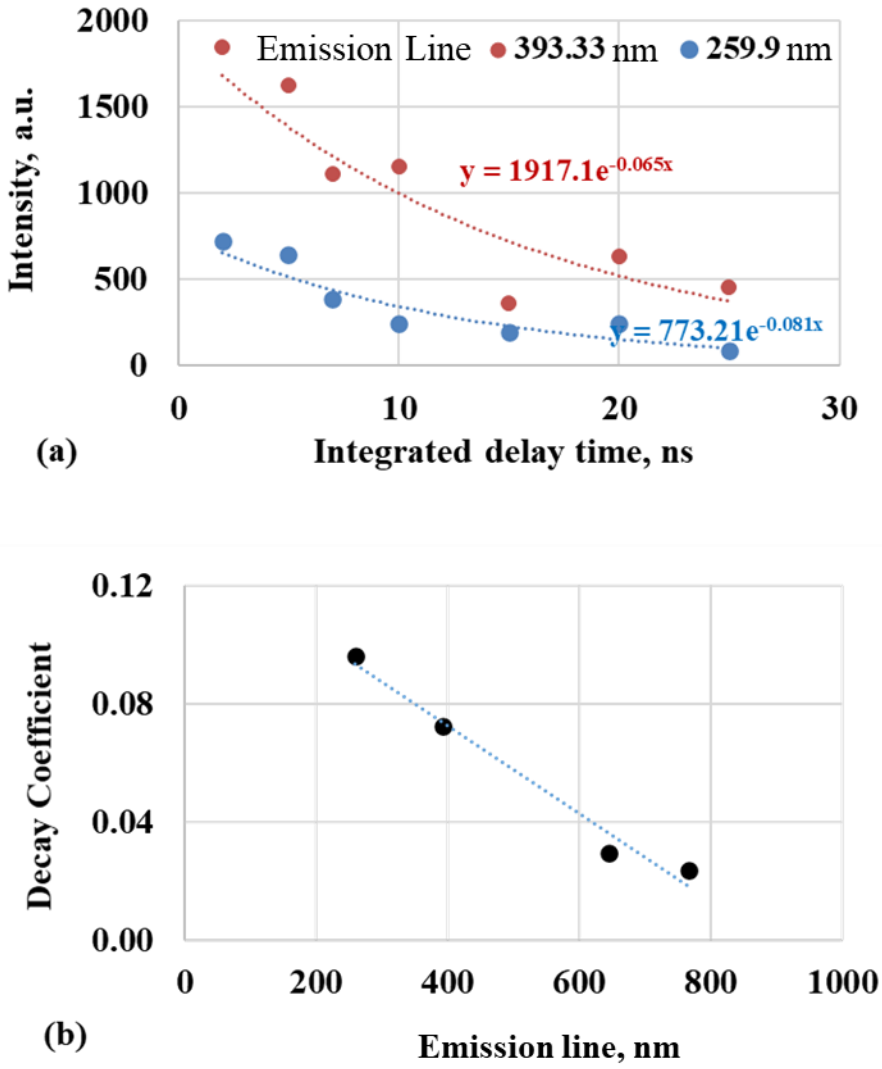

Figure 14: (a) Example plots of intensity versus integrated delay time of two different emission lines; one at 393.3 nm and the other one at 259.9 nm. Intensity on the y-axis is exponentially attenuated as a function of integrated delay time on the x-axis. The decay trends vary for different emission lines and decay coefficients were acquired based on each curve. (b) Plot of decay coefficient versus wavelength. A negative correlation between attenuation factor and emission line is observed. This becomes more important for carbon; since, carbon's major emission lines are at short wavelengths (192-245 nm), the attenuation effect becomes greater. Therefore, selecting optimal integrated delay time is crucial especially for organic rich samples.

2.2.3 Inversion results

After spectra intensities were normalized using the partial least square regression (PLS) method, the spectra were used to create a quantitative inversion. The inversion provided elemental

abundances of carbon, magnesium, silicon, calcium, aluminum, potassium, and iron. Instead of using a specific peak, one or more spectrum windows were selected for each element. This overcame two technical challenges: 1) each element may have several emission lines, and 2) adjacent elements may have overlapping emission lines. Selecting spectral windows for each element is based on the LIBS NIST database (physics.nist.gov). A 150 sample training set from various formations allowed the development of reasonable inversion with a broad range of elemental abundances. **Fig. 15** shows the inversion correlation for each element. For six elements (silicon, calcium, aluminum, potassium, magnesium, iron) LIBS and XRF concentrations show strong correlations with R^2 values above 0.9. For carbon, both inorganic and organic, LIBS concentration and LECO® (without acidizing) concentration show reasonably good correlation with an R^2 of 0.82. **Fig. 16** shows the results from the 100 sample validation dataset: 20 samples were used for total carbon validation, compared to LECO® measures without acidizing, and 80 samples were used for the validation of the rest of elements, compared to XRF measurement. They show reasonably good correlations between LIBS measures and either XRF or LECO® measures, except for iron. The reason that iron shows a poor correlation is mainly due to the non-uniform dispersion of pyrite within organic rich samples.

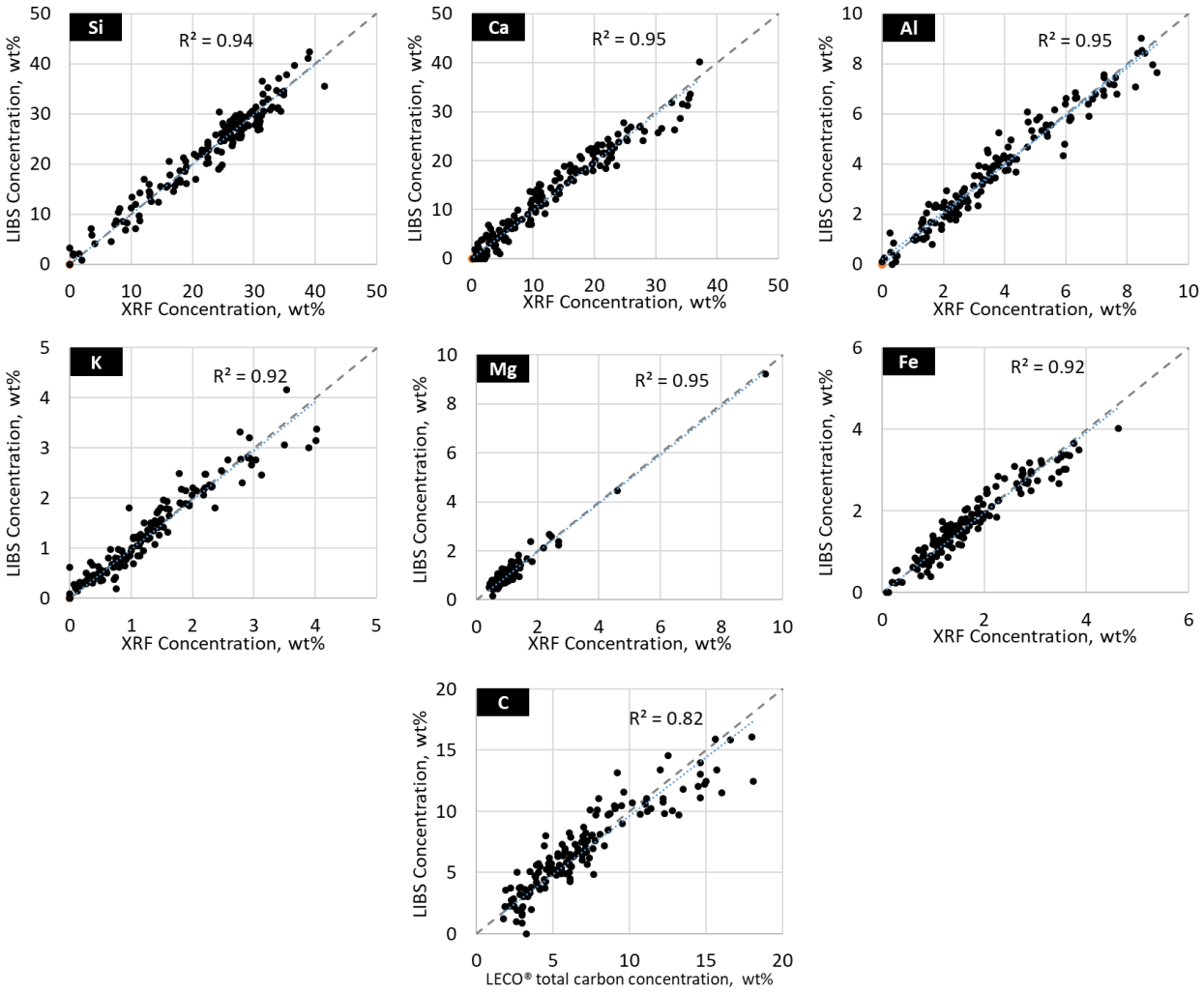

Figure 15: LIBS inversion results of training dataset. For six elements including silicon, calcium, aluminum, potassium, magnesium, and iron, LIBS and XRF concentrations show strong correlations with R^2 values above 0.9. For carbon (including both inorganic and organic), LIBS and LECO®(without acidizing) concentrations show reasonably good correlation with an R^2 of 0.82.

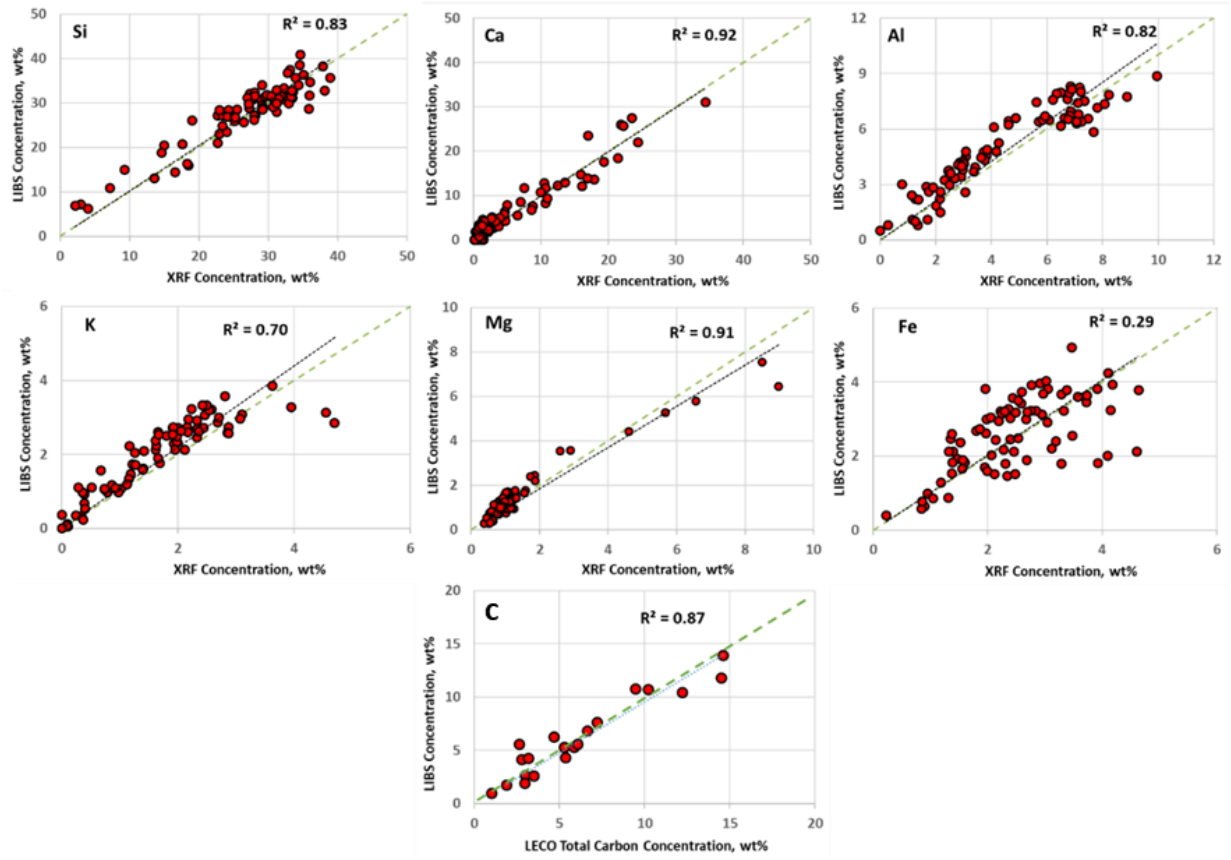

Figure 16: LIBS validation dataset inversion results. 20 samples were used for total carbon validation, compared to LECO® measures without acidizing, and 80 samples were used for the validation of the rest of elements, compared to XRF measurement. They show reasonably good correlations between LIBS measures and either XRF or LECO® measures, except for iron. The reason that iron shows a poor correlation is mainly due to the non-uniform dispersion of pyrite within organic rich samples.

2.2.4 Total organic carbon

LIBS detects total carbon, both inorganic and organic. In order to acquire organic carbon abundance, an additional processing is required. **Fig. 17** shows the workflow to estimate organic carbon abundance. Using internal inversion for mineralogy, elemental data from XRF or LIBS can be converted into mineralogy and total concentration of carbonates (calcite, dolomite, siderite) can be estimated. Inorganic carbon abundance is calculated from total carbonate concentration. By subtracting inorganic carbon from LIBS total carbon measures, TOC can be estimated.

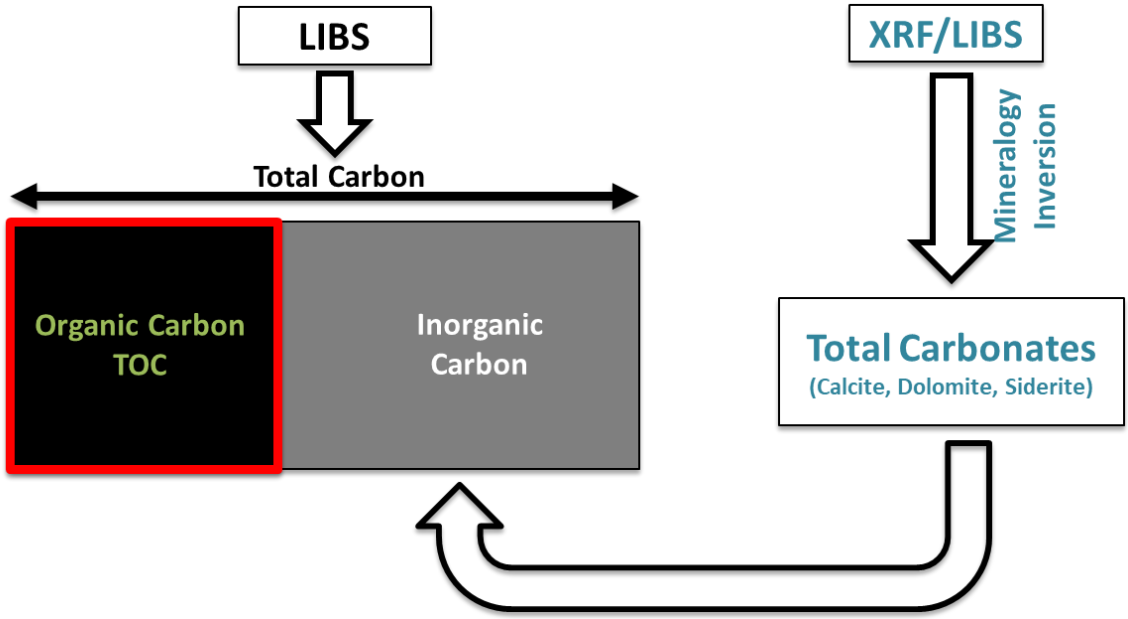

Figure 17: A workflow to estimate organic carbon from LIBS. Elemental data from XRF or LIBS can be converted into mineralogy using internal inversion and total carbonates concentration including calcite, dolomite and siderite can be estimated. By subtracting inorganic carbon from carbonates concentration from LIBS total carbon measure, organic carbon concentration or TOC can be estimated.

In order to precisely compute total organic carbon, total carbonate estimation must be accurate. Total carbonate concentrations converted from XRF elemental data using internal inversion was compared to measured transmission Fourier Transform Infrared (FTIR) mineralogy. FTIR gives a quantitative mineralogy measurement. Compared to the classic method for the mineralogy quantification, X-Ray diffraction (XRD), FTIR overcomes technical challenges in sample preparation and data acquisition (Harville and Freeman, 1988; Sondergeld and Rai, 1993; Herron et al., 1997; Ballard, 2007; Herron et al., 2014). **Fig. 18** shows the comparison of total carbonate weight percentage between calculated concentrations from XRF elemental data and FTIR mineralogy, with XRF on the y-axis and FTIR mineralogy on the x-axis. The correlation has about a 10% error. Finally, **Fig. 19** shows the TOC correlation between XRF-LIBS estimation from the

workflow depicted in **Fig. 17** and LECO® TOC measurement (with acidizing) from the validation dataset. Most of dataset are within ± 2wt% range.

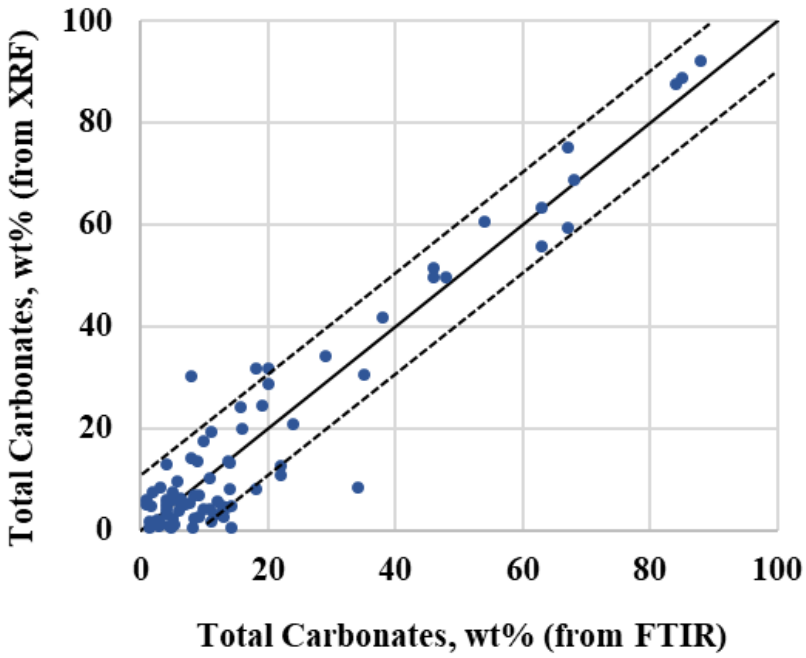

Figure 18: Total carbonate correlation between XRF calculated mineralogy on the y-axis and FTIR measured mineralogy on the x-axis. Total carbonate includes calcite, dolomite, and siderite. It shows reasonably good correlation within 10% of error.

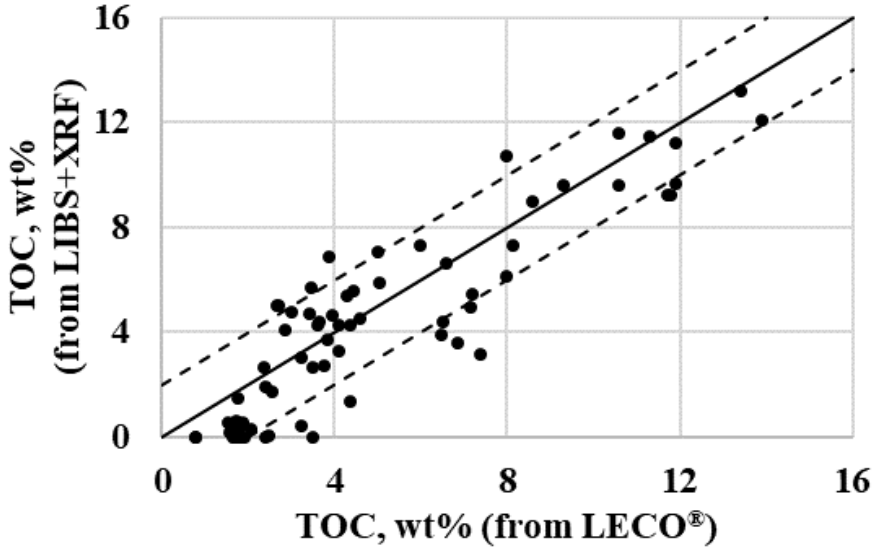

Figure 19: TOC correlation between XRF-LIBS estimation processed by the workflow and LECO® TOC measurement (with acidizing).

Chapter 3: Results and discussion

Elemental analysis was conducted on 8 different cores from Mississippian Meramec in Anadarko basin, OK. As depicted in **Fig. 4**, there are two cross sections; one is from well A to well G (**Fig. 4-a**) and the other one is from well H to well G (**Fig. 4-b**). Section 3.1 to 3.6 will discuss the results following the (a) direction using XRF elemental data and section 3.7 will discuss the result following the (b) direction mainly using LIBS elemental data; both follow the depositional direction from northwest to southeast.

3.1 Synthetic gamma ray

Gamma ray (GR) logs are useful in identifying lithologies. Also, fluctuations in GR are indicators of sea level changes related to the depositional environment. GR is also useful in correlating depths between wells. Ellis and Singer (2007) calculated a synthetic GR from XRF data using equation 2. Driskill et al. (2018) demonstrated that synthetic GR calculated from XRF data correlates well with the core and wireline GRs.

$$Gr\ synthetic = 16 * K(w\%) + 8 * U(ppm) + 4 * Th(ppm) \qquad Eq.2$$

The equation was applied to the dataset and **Fig. 20** shows the comparison between log GR and synthetic GR. Data for each well is divided into three tracks. The first track shows log GR in red, and the synthetic GR in color-graded yellow with darker shades representing a higher GR. Synthetic GR is smoothed over 2 ft to be equivalent with log resolution. The second track is depth in ft, and the third track shows clay index which is the ratio Al over Si from XRF elemental data. Synthetic GR and log GR agree well, and clay index also shows a good correlation with gamma ray response. Well A on the left to well G on the right follows the depositional direction and

synthetic GR also increases. Log GR and clay index also show an increase with the depositional direction.

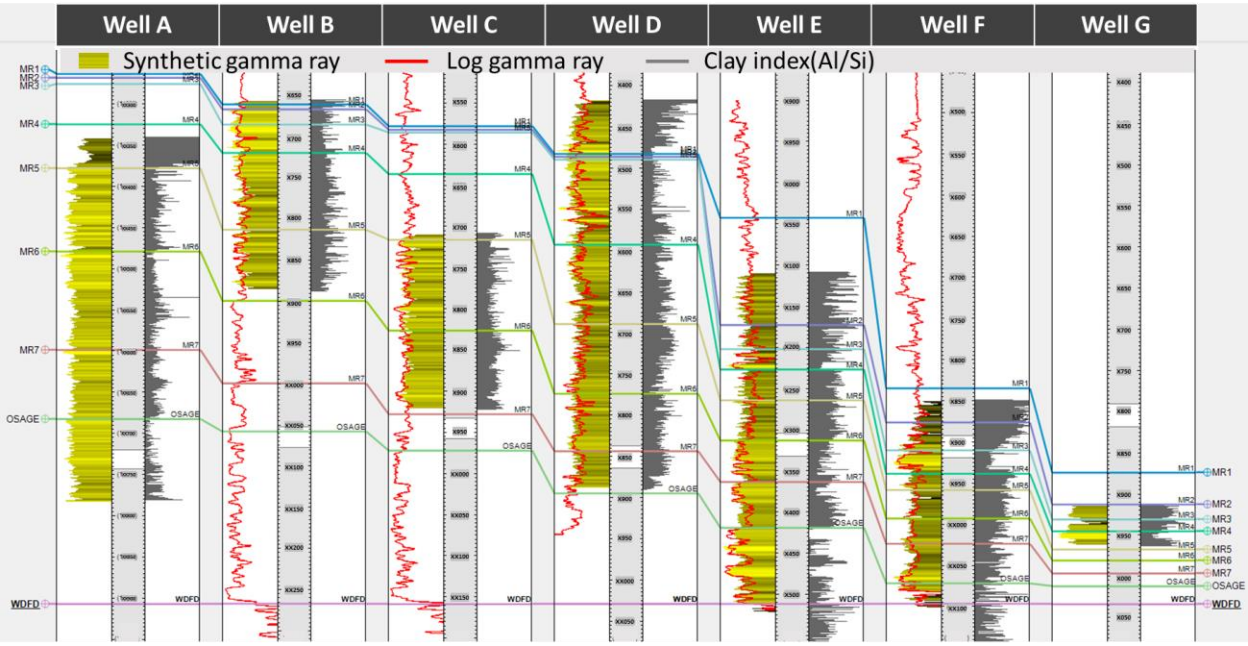

Figure 20**: The comparison between log GR and synthetic GR calculated from XRF data using equation 2. The first track indicates log GR in red, and synthetic GR in color-graded yellow with darker shades representing a higher GR. Synthetic GR is smoothed over 2 ft to be equivalent to log resolution. Second track shows the depth in ft and the third track represents clay index which is the ratio of Al over Si acquired from XRF data. Log GR and synthetic GR agree well, and clay index also follows the same trend. From well A to well G following the depositional direction, both GRs and clay index increase.**

3.2 Mineralogy

Mineralogy is an important factor controlling petrophysical properties and is crucial for defining hydraulic fracturing zones. Major elements such as silicon, aluminum, calcium, magnesium, sodium, potassium, iron, and sulfur are being used as proxies to invert for mineralogy including quartz, carbonates (calcite, dolomite, and siderite), feldspars and clays. Using our internal inversion program, elemental concentrations were inverted to mineralogy concentrations and **Fig.**

21 shows the comparison results with FTIR mineralogy. X-axis indicates FTIR mineralogy in weight % and y-axis indicates XRF mineralogy converted from elemental data in weight % and data are colored by wells. Carbonates include calcite, dolomite, and siderite. Clays include illite, smectite, kaolinite, chlorite. Overall, they show a reasonably good correlation.

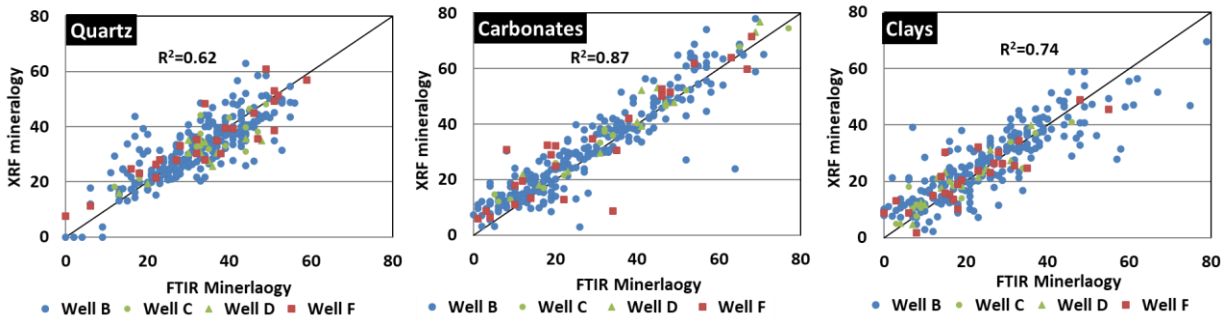

Figure 21: The comparison of mineralogical compositions between XRF-mineralogy which is inverted from elemental data using internal inversion on the y-axis and FTIR mineralogy on the x-axis. Three different groups of mineralogy are shown, and data are colored by wells. Mineralogies are reported as weight percentages. Overall, they show a reasonably good correlation.

Fig. 22 shows the high resolution mineralogy profiles converted from elemental data. The first track is synthetic GR shown previously in **Fig. 20**, with darker shades of yellow representing higher GR. The second track is depth of core in ft, and the third track shows mineralogy. Each mineral indicated in a different color; from left to right, quartz in yellow, dolomite in purple, calcite in cyan, feldspars in orange, and clays in gray. Following the depositional direction from well A on the left to well G on the right, clay concentration increases, and calcite concentration decreases. Also, in proximal direction, closer to the source, heterogeneity is greater than in more distal wells; well A shows very high heterogeneity captured by the fluctuation in the mineralogy profile.

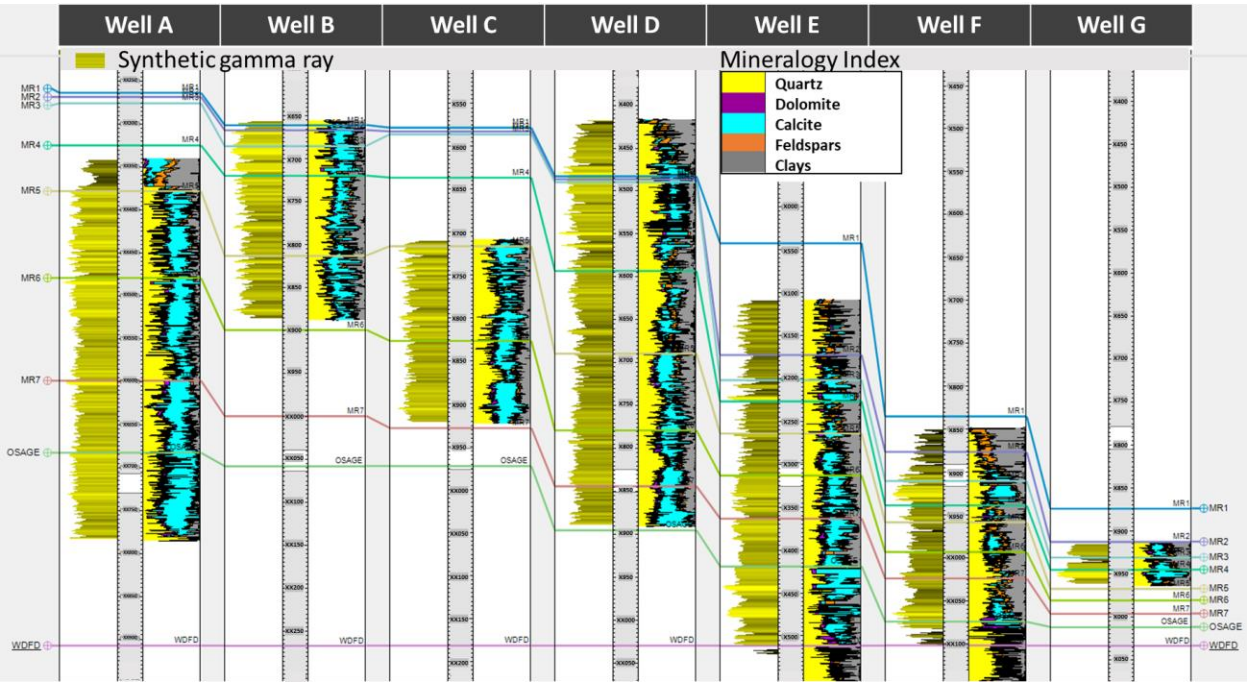

Figure 22: The mineralogy profiles converted from XRF elemental data using our internal inversion program. The first track is synthetic GR, second track is depth in ft, and the third track represents mineralogy profiles. Each mineral is indicated in a different color; from left to right, quartz in yellow, dolomite in purple, calcite in cyan, feldspars in orange, and clays in gray. Following the depositional direction from well A to well G, clay concentration increases, and calcite concentration decreases. Clay concentration and synthetic gamma ray follow also increase from well A to well G.

3.3 Carbonate diagenesis

Core descriptions document the presence of calcite cement. Point count petrographic analyses (from Dr. R. Larese) show carbonate diagenesis is critical to understanding the Meramec formation. **Fig. 23** shows examples of thin section images from two different samples; (a) is from well C and (b) is from well D. Petrographic analyses show that the average calcite cement abundance varies from 9 to 17 volume % in the proximal clastic specimens and 3 to 4 volume % in the progressively more argillaceous distal specimens.

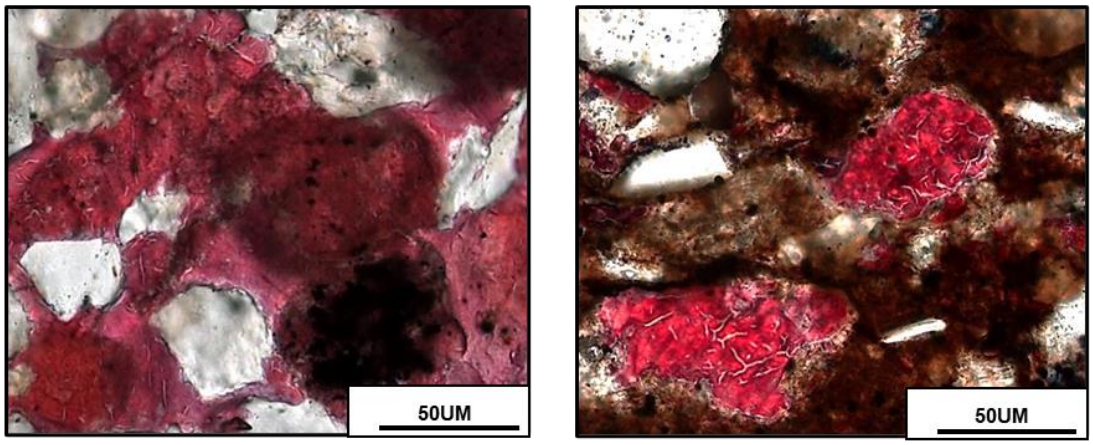

Figure 23: Examples of thin section images from two different samples; (a) is from well C and (b) is from well D (Courtesy of Dr. R. Larese). Petrographic analyses show that the average calcite cement abundance is higher in the proximal clastic specimens than the argillaceous distal specimens. Red alizarin red stain identifies the calcite cement.

Detrital lithic or framework carbonate and diagenetic carbonates showed a positive relationship as shown in **Fig. 24-a. This** implies that diagenetic carbonates are from dissolution of framework carbonates. Price et al. (2020) also point out that calcite cement is a major factor controlling reservoir quality. We attempted to understand the distribution of carbonate diagenesis across the wells using XRF data. The ratio of strontium and calcium has been used as a proxy of carbonate diagenesis (Tucker and Write, 1990; Edgar et al., 2015). **Fig. 24-b** is a plot of diagenetic carbonate determined from petrographic work and Sr-ratio (= Sr/(Ca+Mg)) determined from XRF. It shows a negative relationship. The orange dot was from XRF data measured on the surface of calcite cement vein and it lies on the trend line showing lower value of Sr-ratio. This correlation allows the use of Sr-ratio as an indicator proxy for carbonate diagenesis.

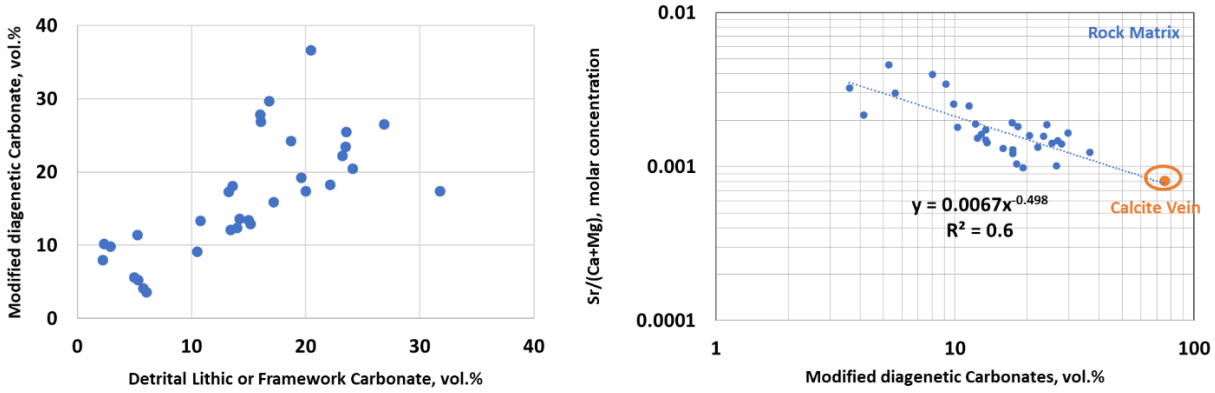

Figure 24: (a) Plot of diagenetic carbonates versus detrital lithic or framework carbonates from point count petrographic analyses (Courtesy of Dr. R. Larese). The two have a positive relationship and it suggests that diagenetic carbonates possibly originate from dissolution of framework carbonates. (b) Plot of Sr-ratio calculated by Sr/(Ca+Mg) in molecular weight versus diagenetic carbonates from point count petrographic analyses (Courtesy of Dr. R. Larese) shows a negative trend. The orange dot was from XRF data measured on the surface of calcite cement vein. This correlation allows the use of Sr-ratio as an indicator proxy for diagenetic carbonate.

The Sr-ratio was applied over all the wells and **Fig. 25** shows the results. Data for each well is divided into five tracks. The first track is synthetic GR calculated from XRF elemental data, the second track is depth of core in ft, the third track is mineralogy profile, the fourth track is calcium concentration in blue, and the last track is the Sr-ratio. Proximal regions to the north were shallow-water environments, and water generally deepens to the south into the basin (Lane, 1978; Lane and De Kyser, 1980; Gutschick and Sandberg, 1983, Price et al., 2020). In the proximal direction, more carbonates are found with smaller values of Sr-ratio. It suggests that the formation has suffered more from carbonate diagenesis. Carbonate diagenesis impacts petrophysical properties such as porosity and it will be discussed later.

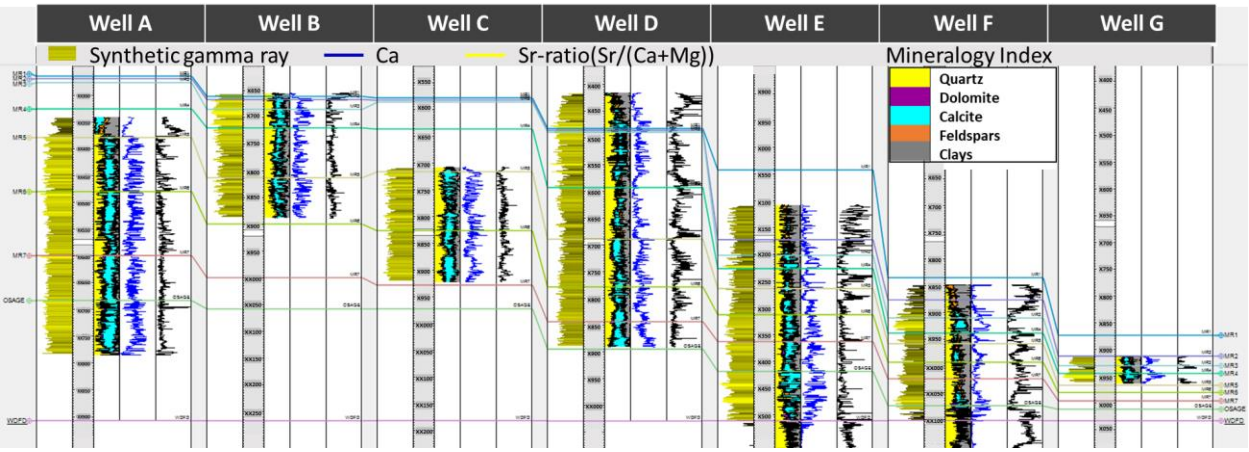

Figure 25: The profiles of carbonate diagenesis across the wells. The first track is synthetic GR calculated from XRF elemental data, the second track is depth, the third track is mineralogy profile, the fourth track is calcium concentration in blue, and the last track is the Sr-ratio, i.e., Sr/(Ca+Mg). In the proximal direction, more carbonates are found with smaller values of Sr-ratio. It suggests that the formation has suffered more from carbonate diagenesis.

3.4 Biogenic quartz and brittleness index

Brittleness of the rock is a major concern when deciding on completion zones and selecting drill bits (Klas et al., 2015; Yacine et al., 2016; Zhang et al., 2017; Das and Chatterjee, 2018; Tang et al., 2018a; Li et al., 2019). Jarvie et al. (2007) computed brittleness index using mineralogy (Equation 3). Using the equation, brittleness index was calculated based on the mineralogy profiles (weight %) inverted from high spatial resolution XRF elemental data.

$$BI = \frac{Quartz + Dolomite}{Quartz + Dolomite + Calcite + Clays} \qquad Eq.3$$

There are proxies that try to differentiate between biogenic quartz and detrital quartz. Biogenic quartz is related with more brittle horizons than detrital quartz. Wright et al. (2010) showed plots of SiO_2 versus Zr from two different formations in shale plays (**Fig. 26-a, b**). Since Zr is one of the terrestrial source proxies (Bhatia and Crook, 1986; Turner, 2016), a positive trend between

SiO_2 and Zr suggests that samples have terrestrial non-biogenic silica. On the contrary, a negative trend suggests that samples have biogenic silica.

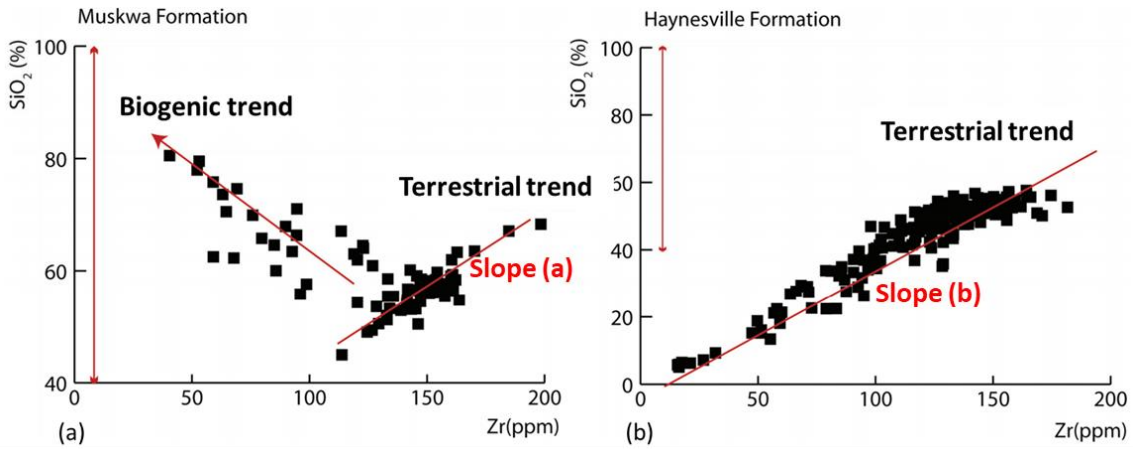

Figure 26: Plots of SiO_2 versus Zr from two different formations; (a) is from Muskwa formation and (b) is from Haynesville formation (Wright et al., 2010). Zr is one of the terrestrial source proxies. Therefore, a positive trend between SiO_2 and Zr suggests that samples have terrestrial non-biogenic silica. On the contrary, a negative trend suggests that samples have biogenic silica. Slope (a) and (b) indicate each trend line of terrestrial trend.

These proxies were applied to entire data set. **Fig. 27** shows the trend between Si and Zr in weight % from well A. Data are colored by different zones in the Meramec. Partial groups of samples from MR4, MR6, MR7, and Osage show the trend of biogenic quartz. Slope *a* and *b* correspond to each slope depicted in Fig. 26. **Fig. 28** shows the profiles of Si and Zr concentration and brittleness index for all the wells. Data for each well is divided into four tracks. The first track is depth in ft, the second track contains mineralogy profiles, and the third track is brittleness index profiles calculated from XRF data using Equation 3. Geologically well B and well C are located close each other. Based on the brittleness index profiles, it can be easily identified that the bottom core from well B is almost identical with the upper part of well C. Finally, the track 4 shows Si concentration in black and Zr concentration in blue in weight %. The area filled in red suggests the presence of

biogenic quartz, i.e., having low Zr concentration with high Si concentration. Well A agrees well with the trend seen in **Fig. 27**.

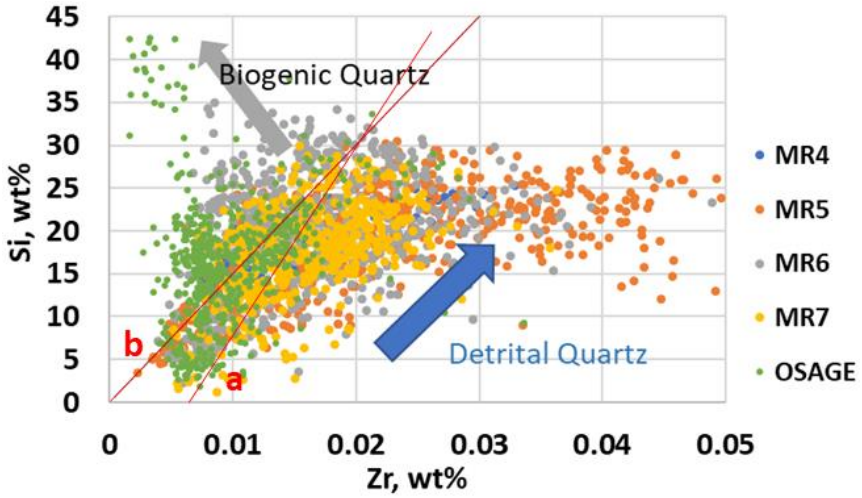

Figure 27: A plot of Si versus Zr from well A. The x-axis is Zr concentration in weight % and y-axis is Si concentration in weight %. Well A contains both biogenic quartz and detrital quartz. Samples are colored by different zones. Partial groups of samples from MR4, MR6, MR7, and Osage show the trend of biogenic quartz. Slope a and b correspond to each slope depicted in Fig. 26.

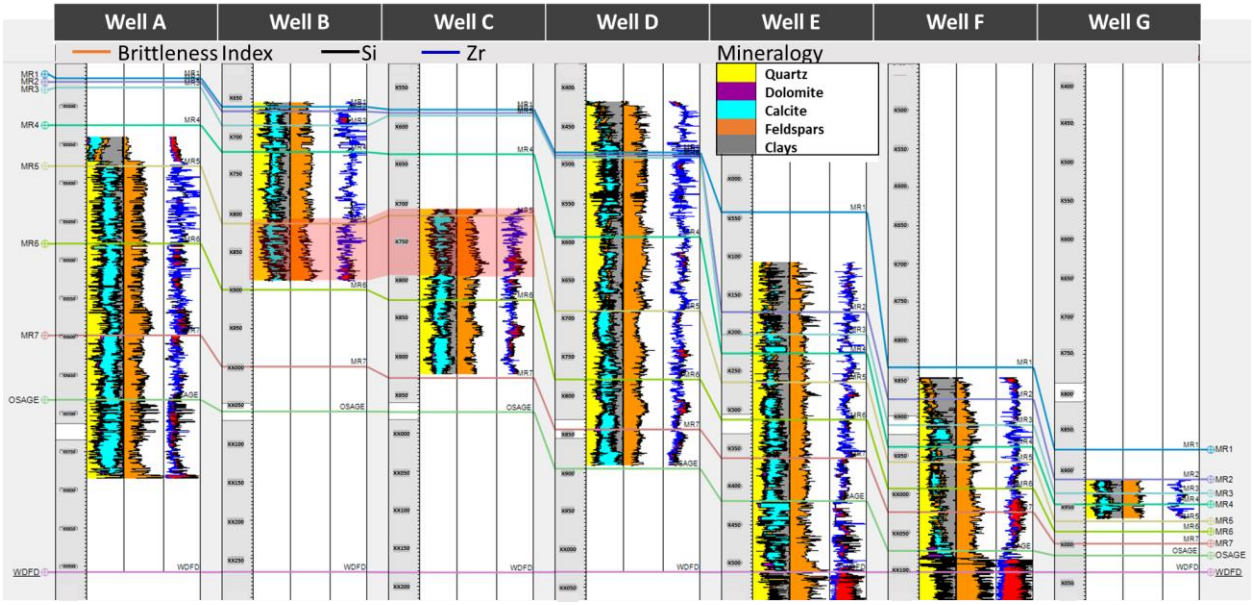

Figure 28: Brittleness index and biogenic quartz profiles. The first track is depth, the second track is mineralogy, and the third track is brittleness index calculated from XRF mineralogy data using Equation 3. Based on the brittleness index profiles, it suggests that the bottom

core from well B is almost identical with the upper part of well C (the area is colored by the transparent red box). The track 4 shows Si concentration in black and Zr concentration in blue in weight %. The area filled in red suggests the presence of biogenic quartz, i.e., having low Zr concentration with high Si concentration.

3.5 Vertical heterogeneity

High spatial resolution XRF data can help capture formation heterogeneity. This becomes important when upscaling to logs and seismics. To quantify the degree of heterogeneity of formation using XRF elemental data, two different spatial scales of Si concentration were used (**Fig. 29**). One is 2-inch scale of the original XRF data, which is shown in red on the second track, and the other is 2-ft scale, which is smoothed using a Gaussian function on the 2-inch data. 2-ft scale of data are closer to the wireline log scale and it is shown in black on second track. A greater discrepancy between these two different scales of data suggests a more heterogenous formation. Therefore, with these two differently scaled of data, the error range was calculated, and it is shown on the third track in purple. Towards the proximal direction, there is greater discrepancy (noise) between the two scaled data sets and greater values of the standard deviation. It suggests that the formation is more heterogeneous. On the contrary, in the distal direction, noise between the two scales and standard deviation decrease, and it suggests that the formations are less heterogeneous.

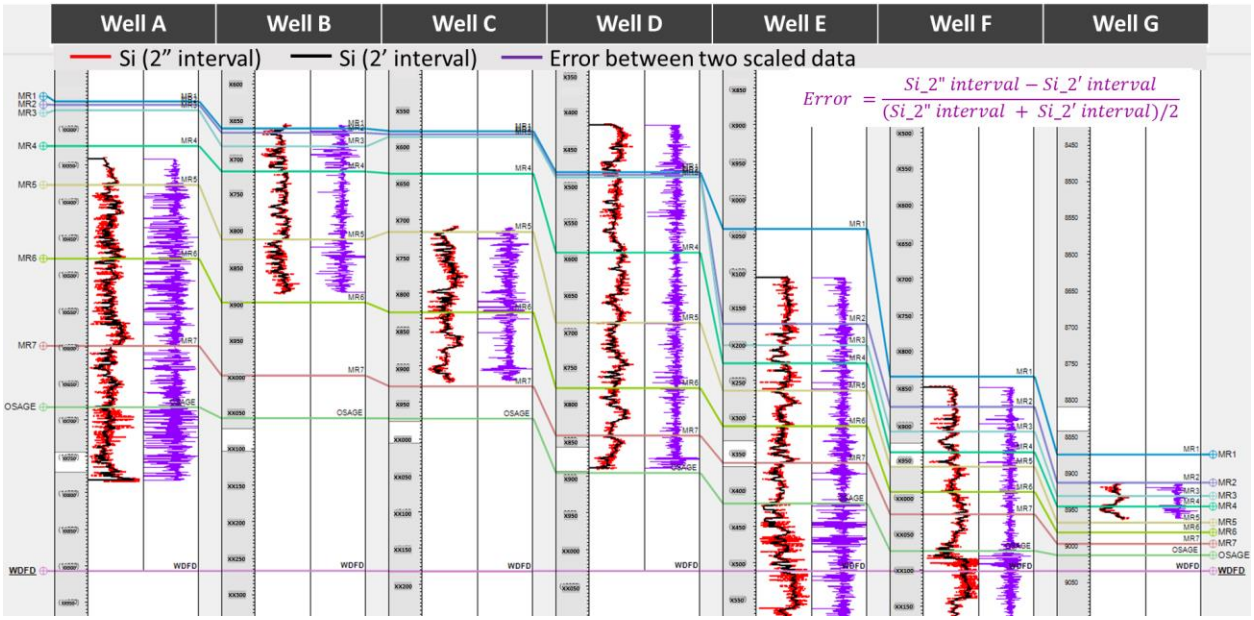

Figure 29: The profile of formation heterogeneity. The first track is depth in ft, the second track has two different scales of Si concentration; One is 2-inch scale of the original XRF data which in red, and the other is 2-ft scale, which is smoothed using a Gaussian function on the 2-inch data in black. 2 ft resolution data are closer to the wireline log scale. The third track is error of these two different scales of data in purple. In proximal direction, greater discrepancies (noise) between the two differently scaled data sets and higher value of standard deviation are found and it suggests that the formation is more heterogeneous.

3.6 Porosity

As briefly mentioned in the previous part on carbonate diagenesis, porosity was measured on 490 plug samples (provided by a service company) from well A, well D, well E and well F. **Fig 30** shows the relationship between porosity and mineralogy inverted from XRF elemental data. It is shown that porosity is controlled by mineralogy (carbonates and clays); porosity decreases as calcite concentration increases and increases as clays concentration increases.

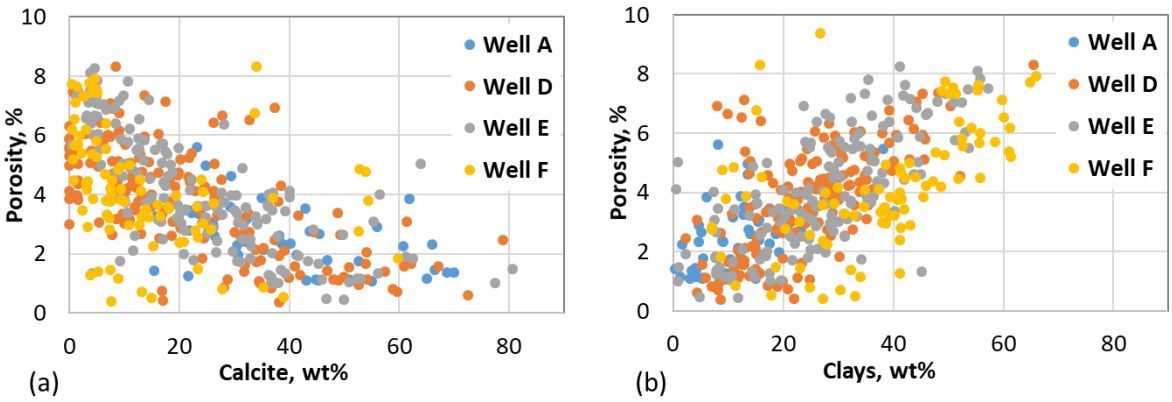

Figure 30: Plots of porosity vs. mineralogy inverted from XRF elemental data. (a) Porosity and calcite concentration have a negative correlation. (b) Porosity and clay concentration have a positive correlation.

Using the data from 450 plug samples, two different analyses were performed; one is clustering analysis and the other is regression analysis. For the clustering analysis, unsupervised clustering K-Means method was conducted using XRF data (11 elements and 5 minerals inverted from XRF elemental abundances) and three facies were acquired. **Fig. 31** shows the distribution of mineralogy and porosity for each facies. Facies 1 in orange has low porosity with high calcite and low clay concentrations. Facies 2 in green has high porosity with low calcite and high clay concentrations. Facies 0 in blue has a composition between facies 1 and 2. These three facies show a good separation. This classification was used to train a model with supervised SVM classification method and applied to the entire dataset of core measurements to predict facies.

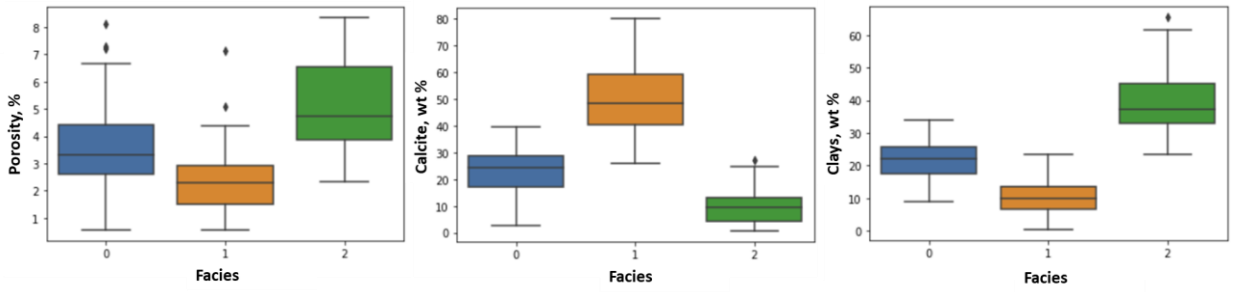

Figure 31: The distribution of porosity and mineralogy (calcite and clays) for each facies resulting from K-Means clustering analysis from 450 plug measurements. Facies 1 in orange has low porosity with high calcite and low clay concentrations. Facies 2 in green has high porosity with low calcite and high clay concentrations. Facies 0 in blue has a composition between facies 1 and 2. These three facies show a good separation.

The other analysis was regression analysis using the same data from 450 plug samples (11 elements and 5 mineral concentrations from XRF data and porosity measurement). Several regression methods were implemented such as linear regression, elastic net regression, etc. Neural network regression method showed the best performance on this dataset. 80% of data were used to build a regression model and the remaining 20% of data were used to validate the model. **Fig 32** shows the results of training set and validation set. The x-axis is measured porosity and the y-axis is predicted porosity. Both training and validation set show reasonably good results with $R^2 > 0.7$.

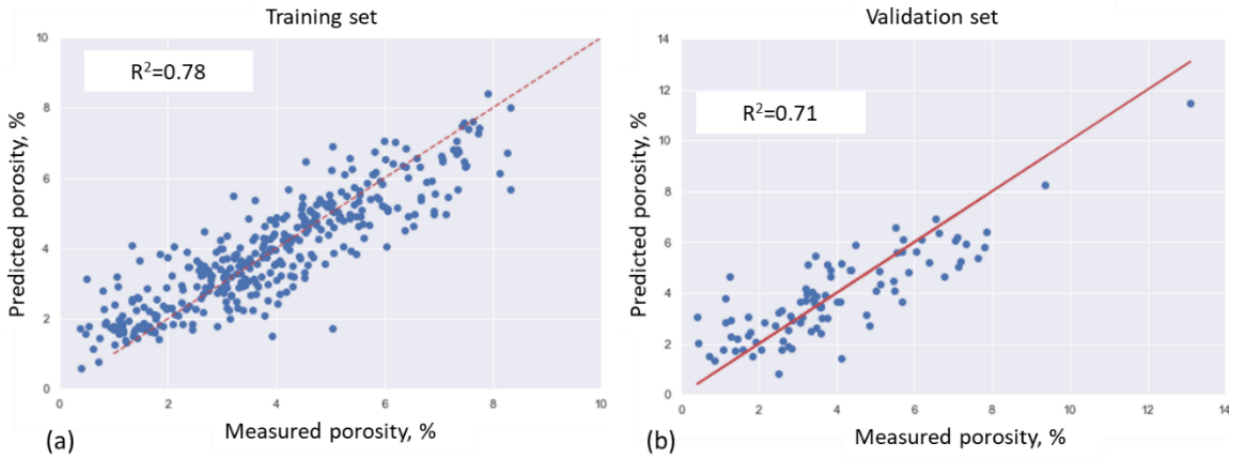

Figure 32: The results of porosity prediction from 450 core measurements. 80% of the data were used to build a prediction model using neural network regression (a) and the remaining 20% of data were used as a validation set (b). The x-axis is measured porosity and the y-axis is predicted porosity from the model. Both training and validation set show reasonably good results with R^2 above 0.7.

Both classification and regression models were applied to entire core XRF data and generated high resolution predicted porosity. **Fig 33** shows the results of facies and predicted porosity values across the wells. Data for each well is divided into four tracks. The first track shows facies, with facies 0 in blue, facies 1 in orange, and facies 2 in green. The second track is depth, and the third track shows mineralogy profiles. The fourth track shows porosity, with predicted porosity from the regression model in black and wireline porosity in red. Predicted porosity and facies agree well with mineralogical composition. Movement in the proximal direction shows greater fluctuation in porosity. **Fig. 34** shows the expanded profiles of well B, C, and D from **Fig. 33** to highlight predicted porosity and log porosity on the fourth track.

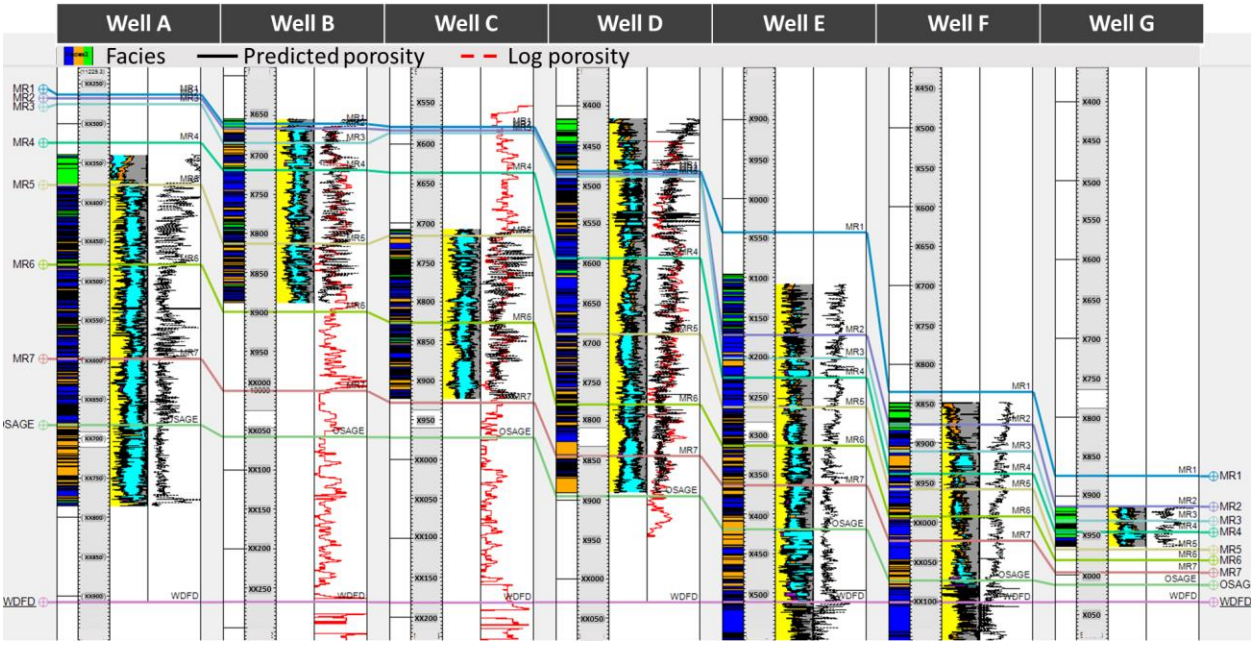

Figure 33: The porosity profiles. The first track shows three facies from classification analysis, with facies 0 in blue, facies 1 in orange, and facies 2 in green. Facies 2 has high clay concentration and low calcite concentration resulting in high porosity. The second track is depth of core in ft, and the third track is mineralogy. The fourth track is porosity with predicted porosity in black from the neural network regression model and wireline porosity in red. Overall, they match well each other.

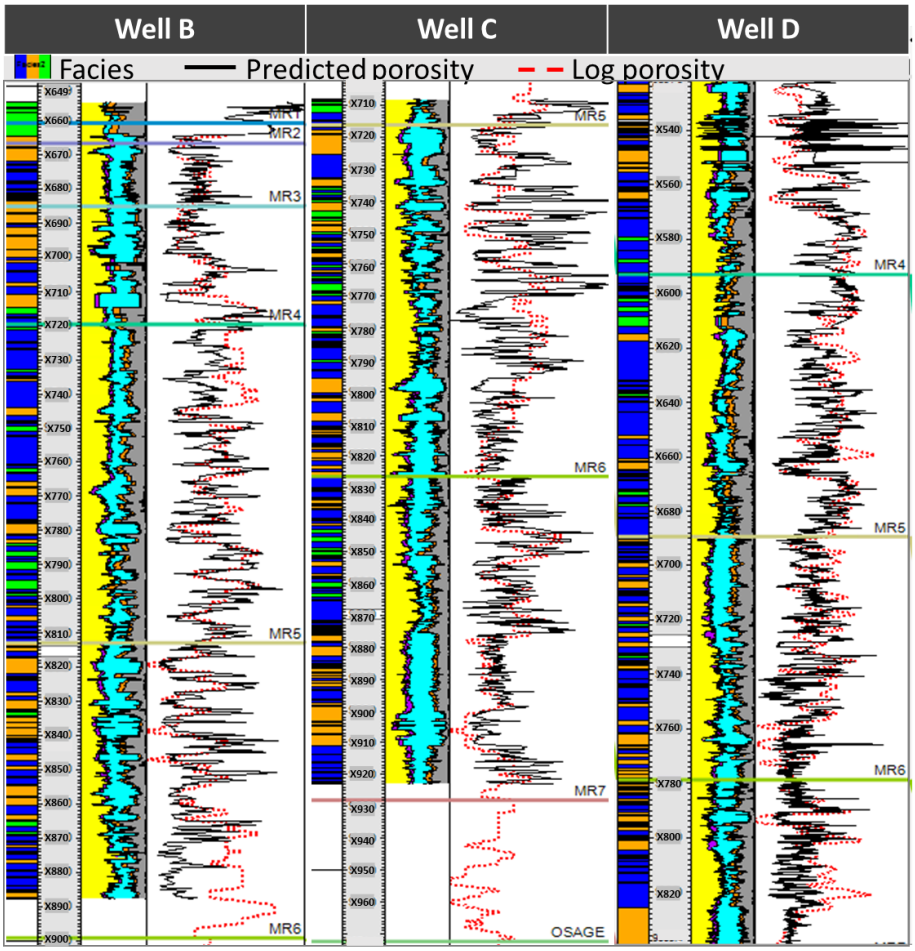

Figure 34: The zoomed profiles of well B, C, and D from Fig. 30. Each track has the same information. The first track shows facies, the second track is depth, the third track is mineralogy, and the fourth track is porosity. The black color in the fourth track indicates predicted porosity and the red dashed line indicates wireline porosity. Overall, they agree well, and predicted porosity provides high spatial resolution profiles.

3.7 Total organic carbon

This section shows the application of LIBS on three cores from well H, well E, and well G. The location of each well is shown in **Fig. 4-b**. The Meramec formation does not have a significant organic carbon content (Coronado, 2018), but we present a general workflow for evaluating organic carbon. Following the workflow depicted in **Fig. 17**, total organic concentration was acquired. **Fig. 35** shows the results. Data for each well is divided into five tracks. The first track shows the synthetic GR, the second track shows the depth, the third track shows mineralogy. The

fourth track is TOC in green ranging 0 to 5 weight%. From well H on the left to well G on the right follows the depositional direction (northwest to southeast). Even though the range of TOC is relatively small and well H and G covers only several zones. In the distal direction, TOC concentration increases. In the same direction, synthetic GR, and clay concentration also increase while calcite concentration decreases. Wang and Gale (2009) updated brittleness index from Jarvie et al. (2007) by adding TOC as a ductile property (**Equation 5**). The fifth track shows the updated brittleness index using **Equation 5.** This method can be more beneficial for organic rich shale samples to acquire high resolution TOC profiles.

$$BI = \frac{Quartz + Dolomite}{Quartz + Dolomite + Calcite + Clays + TOC} \qquad Eq.5$$

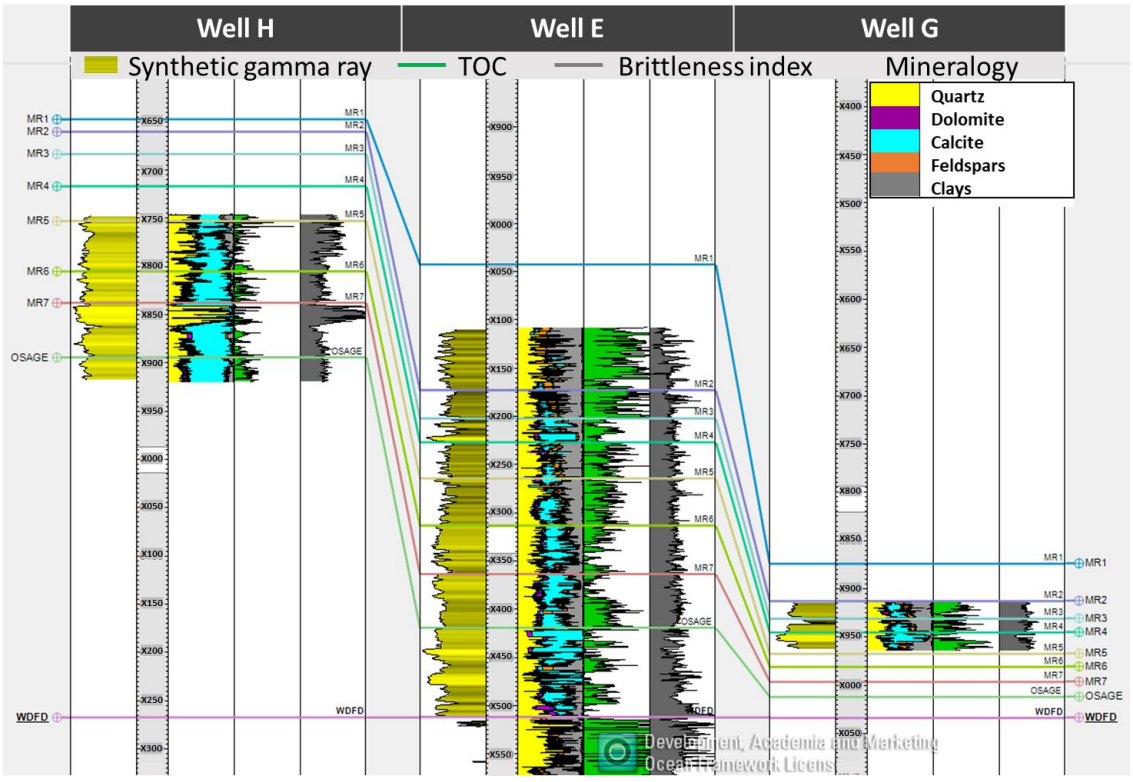

Figure 35: The TOC profiles across the wells. The first track is the synthetic GR, the second track is depth, the third track is mineralogy, the fourth track is TOC (ranging 0 to 5 wt%), and the fifth track is brittleness index using Equation 4. From well H to well G follows

depositional trend. In distal direction, TOC increases, and synthetic GR and clays concentration also increase while calcite concentration decreases.

Chapter 4: Summary and Conclusions

XRF and LIBS high resolution spatial scans were performed on eight cores from the Mississippian Meramec in STACK plays. 16,162 XRF measurements and 2,421 LIBS measurements were acquired, and they were used for elemental analysis. The depositional trend is from northwest to southeast and the water level deepens following the direction from shallow-water condition in the north. In proximal direction more calcareous facies can be found, and as transportation velocity decreases, argillaceous facies can be found. The presence of carbonate diagenesis is a key factor in controlling the reservoir quality in this formation. In the depositional direction, the formation suffered less carbonate diagenesis and the formation becomes less heterogeneous. Based on present study, I draw the following conclusions:

1. Automated rapid scanning using a handheld XRF instrument allows the acquisition high spatial resolution elemental data (1-2 inches) much faster than traditional means.
2. XRF inversion for the elemental quantification was calibrated against ICP-OES-MS measurement and it showed an error less than 3 weight %.
3. A robust LIBS elemental inversion was developed and shows good validation results with an average R^2 value of 0.84, except for iron.
4. A workflow for total organic carbon estimation was developed and 83% of data points are within ±2 wgt % error range compared to LECO® TOC measurement.
5. Elemental abundances of samples were inverted into mineralogy profiles, and they showed a trend with clay increasing and calcite decreasing in the depositional direction (NW to SE).
6. Brittleness index was calculated from XRF-mineralogy model and used to identify the zones with biogenic quartz presence using Si and Zr proxies.

7. By integrating point count petrographic analysis with XRF data, Sr-ratio (Sr/(Ca+Mg)) was used to quantify carbonate diagenesis. In depositional direction (NW to SE), the increase of Sr-ratio implies that the formation suffered less carbonate diagenesis.
8. High resolution XRF data was used to assess the heterogeneity of formation. In depositional direction (NW to SE), the formation shows less heterogeneous.
9. TOC from LIBS showed increasing in distal direction, increasing water depth, and GRs and clay index also showed the increasing trend in the same direction.

Recommendations:

- These elemental analyses can be applied not only to conventional cores but also to cuttings. Retrieving core is very costly, whereas cuttings are a by-product of drilling. Even though the depth resolution can be relatively poor compared to core measurements, elemental analysis using cuttings can provide a more intensive areal spatial database since cuttings can be acquired from drilling wells and can be done in real-time.
- TOC parameters were derived from trace elements. However, all of these parameters are indirect estimations of TOC content. The parameters have to be calibrated by shales plays or even by layers. We can create TOC profiles in organic rich shales by integrating XRF and LIBS.
- Conventionally, lithology characterization has been performed by geologists. This type of interpretation is based on petrology including thin section, mineralogy, and grain size. This can be subjective. With integration of rapid elemental/mineralogy data, and thin section analysis using machine learning techniques, lithology characterization can be performed more systematically and in a more objective manner.

References

Aldahan, A., Possnert, G., Scherer, R., Shi, N., Backman, J., and Bostrom, K. 2000. Trace-Element and Major-Element Stratigraphy in Quaternary Sediments from the Arctic Ocean and Implications for Glacial Termination, Journal of Sedimentary Research (2000) 70 (5): 1095–1106.

Algeo, T.J., and Maynard, J.B. 2004. Trace-Element Behavior and Redox Facies in Core Shales of Upper Pennsylvanian Kansas-Type Cyclothems, Chemical Geology, v 206, pp 289-318.

Altamar, R.P., and Marfurt, K. 2015. Mineralogy-Based Brittleness Prediction From Surface Seismic Data: Application to the Barnet Shale, SEG and AAPG, http://dx.doi.org/10.1190/INT-2013-0161.1.

Bathurst, R.G.C. 1971. *Carbonate Sediments and Their Diagenesis*: Elsevier, New York, pp. 321-543.

Ballard, B.D. 2007. Quantitative Mineralogy of Reservoir Rocks Using Fourier Transform Infrared Spectroscopy, Society of Petroleum Engineers. doi:10.2118/113023-STU

Banner, J.L. 1995. Application of the Trace Element and Isotope Geochemistry of Strontium to Studies of Carbonate Diagenesis. Sedimentology, 42, 805-824.

Beckhoff, B., Kanngieber, B., Langhoff, N., Wedell, R., and Wolff, H. 2006. *Handbook of Practical X-ray Fluorescence Analysis*, Springer, New York.

Bhatia, M.R., and Crook, K.A.W. 1986. Trace Element Characteristics of Graywackes and Tectonic Setting Discrimination of Sedimentary Basins. Contributions to Mineralogy and Petrology, 92, 181-193

Blakey, R. 2011. Paleogeography and geologic evolution of North America, http://cpgeosystems.com/paleomaps.html, (accessed 2014).

Bolger, J.A. 2000. Semi-Quantitative Laser Induced Breakdown Spectroscopy for Analysis of Mineral Drill Core, Appl. Spectrosc. 54 (2000) 181–189.

Bustamante, M. F., Rinaldi, C. A., and Ferraro, J.C. 2001. Laser Induced Breakdown Spectroscopy of Ca in a Soil Depth Profile, Spectrochim. Acta Part B 57B (2001) 303–309.

Clift, P., Wan, S., and Blusztajn, J. 2014. Reconstructing Chemical Weathering, Physical Erosion and Monsoon Intensity Since 25 Ma in the Northern South China Sea: A Review of Competing Proxies. Earth Sci Rev 130:86–102. doi:10.1016/j.earscirev.2014.01.002

Choquette, P.W. and Pray, L.C. 1970. Geologic Nomenclature and Classification of Porosity in Sedimentary Carbonates, AAPG Bulletin, v.54, No. 2, p.207-250

Coronado, D.E.D. 2018. Rock Characterization and Stratigraphy of the Mississippian Strata, Meramec/Sycamore Merge Play, Central Oklahoma, M.S. thesis, The University of Oklahoma

Craddock, P.R., Herron, M.M., and Herron, S.L. 2016. Quantitative Mineral Analysis of Sedimentary Formations Using FTIR Spectroscopy, SPWLA 57th Annual Logging Symposium, June 25-29, 2016

Cremers, D.A., and Radziemski, L.J. 1983. Detection of Chlorine and Fluorine in Air by Laser-Induced Breakdown Spectrometry, Anal. Chem, 55, 1252–1256.

Cremers, D.A., Radziemski, L.J., and Loree, T.R. 1984. Spectrochemical Analysis of Liquids Using the Laser Spark, Appl. Spectrosc, 38, 721–729.

Croudace, I.W., and Rothwell, R.G. 2015. *Micro-XRF Studies of Sediment Cores*, Springer.

Das, B., and Chatterjee, R. 2018. Mapping of Pore Pressure, In-Situ Stress and Brittleness in Unconventional Shale Reservoir of Krishna-Godavari Basin. J. Nat. Gas Sci. Eng. 50, 74–89.

Deguchi, Y., and Wang, Z. 2016. Industrial Applications of Laser Induced Breakdown Spectroscopy: Inteck P401-426; http://dx.doi.org/10.5772/61915

Driskill, B., Pickering J., and Rowe, H. 2018. Interpretation of High Resolution XRF data from the Bone Spring and Upper Wolfcamp, Delaware Basin, USA: URTeC 2901968.

Edgar, K.M., Anagnostou, E., Pearson, P.N., and Foster, G.L. 2015. Assessing the Impact of Diagenesis on d11B, d13C, d18O, Sr/Ca and B/Ca Values in Fossil Planktic Foraminiferal Calcite, Elsevier, Geochimica et Cosmochimica Acta 166 (2015) 189–209.

Effenberger, A.J. and Scott, J.R. 2010. Effect of Atmospheric Conditions on LIBS Spectra: Sensor 2010, 10, 4907-4925, https://www.ncbi.nlm.nih.gov/pmc/articles/PMC3292154

Ellis, D.V., and Singer, J.M. 2007. *Well logging for Earth Scientists*, Springer, Heidelberg, 692 p.

Frazier, W.J., and Schwimmer, D.R. 1987. *Regional stratigraphy of North America*: New York, Plenum Press,719 p., doi:10.1007/978-1-4613-1795-1.

Gottfried, J.L., Harmoon, R.S., De Jucia Jr, F.C., and Miziolek, A.W. 2009. Multivariate Analysis of Laser-Induced Breakdown Spectroscopy Chemical Signatures for Geomaterial Classification, ELSEVIER, Spectrochimica Acta Part B 64 (2009) 1009–1019

Grant, K.J., Paul, G.L., and O'Neill, J.A. 1991. Quantitative Elemental Analysis of Iron Ore by Laser Induced Breakdown Spectroscopy, Appl. Spectrosc. 45 (1991) 701–705

Gutschick, R.C., and Sandberg, C.A. 1983. Mississippian continental margins of the conterminous United States, in D. J. Stanley and G. T. Moore, eds., The Shelfbreak: Critical interface on continental margins: Tulsa, Oklahoma, SEPM Special Publication 33, p. 79–96, doi: 10.2110/pec.83.06.0079.

Han, H., Dang, S., Acosta, J., Fu, J., Sondergeld, C., and Rai, C. 2019. X-Ray Fluorescence and Laser-Induced Breakdown Spectroscopy for Advanced Rock Elemental Analysis, URTeC, https://doi.org/10.15530/urtec-2019-1072.

Hardisty, L. 2019. Stratigraphic Variability of Mississippian Meramec Chemofacies and Petrophysical Properties Using Machine Learning and Geostatistical Modeling, STACK

Trend, Anadarko Basin, Oklahoma, M.S. Thesis, University of Oklahoma, Norman, Oklahoma.

Hart, N.R., Dix, M.C., Mainali, P., Rowe, H.D., Morrell, A., and Matheny, M. 2019. Modeling Mineralogy and Total Organic Carbon (TOC) from X-Ray Fluorescence (XRF) Elemental Data from Improved Formation in the Powder River Basin, URTeC, DOI 10.15530/urtec-2019-584

Harville, D.G. and Freeman, D.L. 1988. The Benefits and Application of Rapid Mineral Analysis Provided by Fourier Transform Infrared Mineralogy, SPE 18120, 141-150.

Harmon, R.S., DeLucia, F.C., McManus, C.E., McMillan, N.J., Jenkins, T.F., Walsh, M.E., and Miziolek, A. 2006. Laser-Induced Breakdown Spectroscopy-An Emerging Chemical Sensor Technology for Real-Time Filed-Portable, Geochemical, Mineralogical, and Environmental Application, ELSEVIER, Applied Geochemistry 21 (2006) 730–747

Herron, M. M., Matteson, A., and Gustavson, G. 1997. Dual-Range FT-IT Mineralogy and the Analysis of Sedimentary Formations, SCA-9729, 12pp.

Herron, S, Herron, M., Pirie, I., Saldungaray, P., Craddock, P., Charsky, A., Polyakov, M., Shray, F., and Li, T. 2014. Application and Quality Control of Core Data for the Development and Validation of Elemental Spectroscopy Log Interpretation, SPWLA 55th Annual Logging Symposium, May 18-22., paper LLL.

Hevesy, V.G. *1932. Chemical Analysis by X-rays and Its Applications*. McGrawHill, New York.

Hilbk-Kortenbruck, F., Noll, R., Wintjens, P., Falk, H., and Becker, C. 2001. Analysis of Heavy Metals in Soils Using Laser Induced Breakdown Spectroscopy Combined with Laser Induced Fluorescence, Spectrochim. Acta Part B 56B (2001) 933–945.

Hildred, G.V., Ratcliffe, K.T., Wright, A.M., Zaitlin, B.A., and Wray, D.S. 2010. Chemostratigraphic Applications to Low-Accommodation Fluvial Incised-Valley Settings: An Example for the Lower Mannville Formation of Alberta, Canada, Journal of Sedimentary Research, v 80, pp 1032-1045.

Jaccard, S.L., Haug, G.H., Sigman, D.M., Pedersen, T.F., Thierstein, H.R., and Röhl, U. 2005. Glacial/Interglacial Changes in Subarctic North Pacific stratification, Science 308:1003–1006. doi:10.1126/science.1108696.

Jain, J., Hartzler, D., McIntyre, D., Moore, J, and Crandall, D. 2019. Laser Induced Breakdown Spectroscopy: An Emerging Spectroscopic Technique for Shale Rock Characterization, URTeC, DOI 10.15530/urtec-2019- 389.

Jarvie, D.M., Hill, R.J, Ruble, T.E., and Pollastro, R.M. 2007. Unconventional Shale-Gas Systems: The Mississippian Barnett Shale of North-Central Texas as One Model for Thermogenic Shale-Gas Assessment: AAPG Bulletin, 91, 475–499, DOI: 10.1306/12190606068.

Jenkins, R. 1988. *X-ray fluorescence spectrometry*, John Wiley & Sons, New York, https://doi.org/10.1002/xrs.1300180411

Jenkins, R., Gould, W.R., and Gedcke, D. 1995. *Quantitative X-ray Spectrometry*, Marcel Dekker, Inc., New York.

Jenkins, R. 1999. *X-ray Fluorescence Spectrometry*, Second Edition, Wiley-Interscience, New York.

Jenkyns, H.C. 2010. Geochemistry of Oceanic Anoxic Events, Geochemistry Geophysics Geosystems, v 11, pp 1-30.

Klas, E., Maharidge, R., and Hurt, R. 2015. Mechanical Versus Mineralogical Brittleness Indices Across Various Shale Plays, SPE Annual Technical Conference and Exhibition Held in Houston, SPE-174781-MS.

Lane, H. R. 1978. The Burlington Shelf (Mississippian, north-central United States): Geologica et Palaeontologica, v. 12, p. 165–175.

Lane, H.R., and Kyser, T.L.D. 1980. Paleogeography of the Late Early Mississippian (Tournasian 3) in the Central and Southwestern United States, in T. D. Fouch and E. R. Magathan, eds., Paleozoic paleogeography of west central United States: Tulsa, Oklahoma, Rocky Mountain Section SEPM, p. 149–159.

Lauterbach, S., Brauer, A., Andersen, N., Danielopol, D., Dulski, P., Hüls, M., Milecka, K., Namiotko, T., Obremska, M., Grafenstein, U., and Participants, D. 2011. Environmental Responses to Late Glacial Climatic Fluctuations Recorded in the Sediments of Pre-Alpine Lake Mondsee (northeastern Alps). J Quat Sci 26:253–267. doi:10.1002/jqs.1448

Li, Y., Long, M., Zuo, L., Li, W., and Zhao, W. 2019. Brittleness Evaluation of Coal Based on Statistical Damage and Energy Evolution Theory, Journal of Petroleum Science and Engineering, 172, pp.753-763.

Liritzis, I., and Zacharias, N. 2010. *Portable XRF of Archaeological Artifacts: Current Research Potentials and Limitations*, Springer, New York, pp. 109-142.

Longman, M.W. 1980. Carbonate Diagenetic Textures from Near Surface Diagenetic Environments: AAPG Bull., V. 64, pp. 461-487.

Markey, A.M., Clark, C.S., Succop, P.A., and Roda, S. 2008. Determination of the Feasibility of Using a Portable X-ray Fluorescence (XRF) Analyzer in the Field for Measurement of Lead Content of Sieved Soil, J. Environ, Health 70, 24-29.

Miller, M. 2019. Mississippian Meramec Lithologies and Petrophysical Property Variability, STACK trend, Anadarko Basin, Oklahoma, M.S. Thesis, University of Oklahoma, Norman, Oklahoma.

Milliman, J.D. 1974. *Marine Carbonates*: Springer-Verlag, New York, pp. 270-313.

Norrish, K., and Chappell, B.W. 1977. X-ray Fluorescence Spectroscopy, Physical Methods in Determinative Mineralogy, pp.201-272.

Norrish, K., and Hutton, J.T. 1969. An Accurate X-ray Spectrographic Method for the Analysis of a Wide Range of Geological Samples, Geochim, Cosmochim, Acta 33, 431-453. http://dx.doi.org/10.1016/0016-7037(69)90126-4.

Northcutt, R.A., and Campbell, J.A. 1996. Geological Provinces of Oklahoma, Oklahoma Geol. Surv. Open File Rep., OF5–95.

Parrish, W. 1956. *X-Ray Spectrochemical Analysis*. Philips Tech. Rev. 17, 269e286.

Pälike, H., Shackleton, N.J., and Röhl, U. 2001. Astronomical Forcing in Late Eocene Marine Sediments. ELSEVIER, Earth and Planetary Science Letters 193 (2001) 589-602

Pearce, T.J., Wray, D.S., Ratcliffe, K.T., Wright, D.K., and Moscariello, A. 2005. Chemostratigraphy of the Upper Carboniferous Schooner Formation, Southern North Sea, in Collinson, J.D., Evans, D.E., Holliday, D., and N. Jones, (eds) Carboniferous Hydrocarbon Geology: The Southern North Sea and Surrounding Onshore Areas, Yorkshire Geological Society Occasional Publication 7, pp 147-164.

Pearce, T.J., and Jarvis, I. 1992. Applications of Geochemical Data to Modelling Sediment Dispersal Patterns in Distal Turbidites: Late Quaternary of the Madeira Abyssal Plain, Journal of Sedimentary Petrology, 62, 1112-1129

Pearce, T.J., Besly, B.M., Wray, D.S., and Wright, D.K. 1999. Chemostratigraphy: A Method to Improve Interwell Correlation in Barren Sequences – a Case Study Using Onshore Duckmantian/Stephanian Sequences (West Midlands, U.K.). Sedimentary Geology, 124, 197-220.

Pe-Piper, G., Triantafyllidis, S., and Piper, D.J.W. 2008. Geochemical Identification of Clastic Sediment Provenance from Known Sources of Similar Geology: the Cretaceous Scotian Basin, Canada, Journal of Sedimentary Research, v 78, pp 595-607.

Perrone, A., Finlayson, J.E., Bartelink, E.J., and Dalton, K.D. 2014. Chapter 7. Application of Portable X-ray Fluorescence (XRF) for Sorting Commingled Human Remains, Commingled Human Remains, https://doi.org/10.1016/B978-0-12-405889-7.00007-1.

Phillips, S.C., and Speakamn, R.J. 2009. Initial Source Evaluation of Archaeological Obsidian from the Kuril Islands of the Russian Far East Using Portable XRF, J. Archaeol. Sci 36, 125-1263

Pollard, M., Batt, C., Stern, B., and Suzanne, M.M.Y. 2007. *Analytical Chemistry in Archaeology*, Cambridge Manuals in Archaeology, Cambridge: Cambridge University Press.

Potts, P.J. 1987. A Handbook of Silicate Rock Analysis, Mineralogical Magazine, doi:10.1180/minmag.1987.051.363.23

Potts, P.J., Webb, P.C., Williams-Thorpe, O., and Kilworth, R. 1995. Analysis of Silicate Rocks Using Field-Portable X-ray Fluorescence Instrumentation Incorporating a Mercury (II) Iodide Detector; A Preliminary Assessment of Analytical Performance, The Analyst 120, 1273-1278.

Potts, P.J., and West, M. 2008. Portable X-ray Fluorescence Spectrometry: Capabilities for In Situ Analysis, The Royal Society of Chemistry, Cambridge.

Price, B.J., Pollack A.C., Lamb A.P., Peryam T.C., and Anderson, J.R. 2020. Depositional Interpretation and Sequence Stratigraphic Control on Reservoir Quality and Distribution in the Mermecian Sooner trend Anadarko Basin, Canadian, and Kingfisher Counties(STACK) Play, Anadarko Basin, Oklahoma, United States, The American Association of Petroleum Geologists, DOI:10.1306/04301917411.

Ramkumar, M. 2015. *Chemostratigraphy Concepts, Techniques, and Applications,* first edition: Elsevier.

Ratcliffe, K.T., Wright, A.M., Hallsworth, C., Morton, A., Zaitlin, B.A., Potocki, D., and Wray, D.S. 2004. An Example of Alternative Correlation Techniques in a Low-Accommodation Setting, Nonmarine Hydrocarbon System: the (Lower Cretaceous) Mannville Basal Quartz Succession of Southern Alberta, American Association of Petroleum Geologists Bulletin, v 88, no 10, pp 1419-1432.

Ratcliffe, K.T., Wright, A.M., Montgomery, P., Palfrey, A., Vonk, A., Vermeulen, J., and Barrett, M. 2010. Application of Chemostratigraphy to the Mungaroo Formation, the Gordon Field, offshore Northwest Australia, Journal of the Australian Petroleum Production and Exploration Association, 50th Anniversary Issue, pp 371-388.

Ratcliffe, K.T., Wright, A.M., and Spain, D. 2012a. Unconventional Methods for Unconventional Plays: Using Elemental Data to Understand Shale Resource Plays, Part 1, Petroleum Exploration Society of Australia (PESA) New Resources, February/March, pp 89-93.

Ratcliffe, K., Wright, M., and Spain, D. 2012b. Unconventional Methods for Unconventional Plays: Using Elemental Data to Understand Shale Resource Plays, Part 2, Petroleum Exploration Society of Australia (PESA) New Resources, April/May. pp 55-60.

Sageman, B.B. and Lyons, T.W. 2004. Geochemistry of Fine-Grained Sediments and Sedimentary Rocks. In: Mackenzie, F. (ed.) Sediments, Diagenesis, and Sedimentary Rock. Treatise on Geochemistyr, 7, 115-158.

Sanghapi, H.K., Jain, J., Bolshakov, A., Lopano, C., Mclntyre, D., and Russo, R. 2016. Determination of Elemental Composition of Shale Rocks by Laser Induced Breakdown Spectroscopy, ELSEVIER, Spectrochimica Acta Part B 122 (2016) 9–14

Scholle, P.A. 1978. A Color Illustrated Guide to Carbonate Rock Constituents, Textures, Cements, and Porosities: AAPG Memoir 27, Tulsa, pp. 129-168.

Shaw, C.H. 1952. Chemical Analysis by X-rays, Ohio J. Sci. 52, 134-145.

Shrivastava, P., O'Connell, S., and Whitely, A. 2005. Handheld X-ray Fluorescence: Practical Application as a screening Tool to Detect the Presence of Environmentally-Sensitive Substances in Electronic Equipment, IEEE International Symposium on Electronics and Environment, pp. 157-162.

Sondergeld, C. H. and Rai, C.S. 1993. A new exploration tool: Quantitative Core Charactertization, PAGEOPH 141, 2/3/4, 249-268.

Svendsen, J., Friis, H., Stollhofen, H., and Hartley, N. 2007. Facies Discrimination in a Mixed Fluvio-Eolian Setting Using Elemental Whole-Rock Geochemistry – Applications for Reservoir Characterization, Journal of Sedimentary Research, v 77, pp 23-33, doi: 10.2110/jsr.2007.008.

Tang, J., Wu, K., Zeng, B., Huang, H., Hu, X., Guo, X., and Zuo, L. 2018a. Investigate Effects of Weak Bedding Interfaces on Fracture Geometry in Unconventional Reservoirs, J. Petro. Sci. Eng. 165, 992–1009.

Treanton, J.A. 2014. Outcrop-derived chemostratigraphy of the Woodford Shale, Murray County, Oklahoma. M.S. thesis, The University of Oklahoma. 83pp.

Tribovillard, N., Algeo, T.J., Lyons, T., and Riboulleau, A. 2006. Trace Metals as Paleoredox and Paleoproductivity Proxies: An Update. Chemical Geology, 232, 12-32.

Tribovillard, N., Bout-Roumazeilles, V., Algeo, T., Lyons, T.W., Sionneau, T., Montero-Serrano, J.C., Riboulleau, A., and Baudin, F. 2008., Paleodepositional Conditions in the Orca Basin as Inferred From Organic Matter and Trace Metal Contents, Marine Geology, v 254, pp 62-72, doi: 10.1016/j.margeo.2008.04.016.

Tucker, M.E and Wrignt, V.P. 1990. *Carbonate Sedimentology*, John Wiley & Sons.

Turgeon, S., and Brumsack, H.J. 2006. Anoxic vs. Dysoxic Events Reflected in Sediment Geochemistry During the Cenomanian-Turonian Boundary Event (Cretaceous) in the Umbria-Marche Basin of central Italy, Chemical Geology, v 234, pp 321-339.

Turner, B.W. 2016. Utilization of Chemostratigraphic Proxies for Generating and Refining Sequences Stratigraphic Frameworks in Mudrocks and Shales, PhD dissertation, University of Oklahoma, Norman, Oklahoma.

Tjallingii, R., Röhl, U., Kölling, M., and Bickert, T. 2007. Influence of the Water Content on X-ray Fluorescence Core Scanning Measurements in Soft Marine Sediments, Geochem Geophys Geosyst8:Q02004. doi:10.1029/2006GC001393

Van-Daele, M., Moernaut, M., Silversmit, G., Schmidt, S., Fontjin, K., Heirman, K., Vandoorne, W., De-Clercq, M., Van Acker, A. , Woolf, C., Pino, M., Urrutia, R., Roberts, S. J., Vincze, L., and De-Batiste, M. 2014, The 600 yr Eruptive History of Villarrica Volcano (Chile) Revealed by Annually Laminated Sediments, Geol Soc Am Bull 126:481–498. doi:10.1130/B30798.1

Wang, F.P., and Gale, J.F.W. 2009. Screening Criteria for Shale-Gas Systems: Gulf Coast Association of Geological Societies Transactions, 59, 779–793.

Washburn, K.E. 2015. Rapid Geochemical and Mineralogical Characterization of Shale by Laser-Induced Breakdown Spectroscopy, ELSEVIER, Organic Geochemistry 83–84 (2015) 114–117

Weissert, H., Joachimski, M., and Sarnthein, M. 2008. Chemostratigraphy, Newsletters on Stratigraphy, 145-179. DOI: 10.1127/0078-0421/2008/0042-0145

Witzke, B.J. 1990. Paleoclimatic Constrains for Paleozoic Paleolatitudes of Laurentia and Euramerica, in W. S. McKerrow and C. R. Scotese, eds., Paleozoic Paleogeography and Biogeography: Geological Society, London, Memoirs 1990, v. 12, p. 57–73, doi:10.1144 /GSL.MEM.1990.012.01.05.

Wright, A.M., Spain, D., and Ratcliffe, K.T. 2010. Application of Inorganic Whole Rock Geochemistry to Shale Resource Plays, CSUG/SPE 137946

Xu, T., Liu, J., Shi, Q., He, Y., Niu, G., and Duan, Y. 2015. Multi-Elemental Surface Mapping and Analysis of Carbonaceous Shale by Laser-Induced Breakdown Spectroscopy, ELSEVIER, Spectrochimica Acta Part B 115 (2016) 31–39

Yacine, K., Lyes, O., Dave, B., and Ouenes, A. 2016. Lithology Constrained Elastic Inversion-Application to Niobrara Brittleness Estimation, SEG International Exposition and 86th Annual Meeting, pp. 4916–4920.

Young, K.E., Evans, C.A., Hodges, K.V., Bleacher, J.E., and Graff, T.G. 2016. A review of the handheld X-ray Fluorescence Spectrometer as a Tool for Field Geologic Investigations on Earth and in Planetary Surface Exploration, ELSEVIER, Applied Geochemistry 72 (2016) 77-87

Zhang, J., Ai, C., Li, Y., Zeng, J, and Qiu, D. 2017. Brittleness Evaluation Index Based on Energy Variation in the Whole Process of Rock Failure. Chinese Journal of Rock Mechanics and Engineering, (6), p.4.

Zurfluh, F. J., Hofmann, B. A., Gnos, E., and Eggenberger, U. 2011. Evaluation of the Utility of Handheld XRF in Meteoritics, X-ray Spectrom, 40, 449-463.

Appendix A : Elemental comparison between XRF and LIBS

Elements including Al, Si, Ca, Mg, K, and Fe from XRF and LIBS are compared in **Fig. 36. Fig. 36 (a)** is from well B and **(b)** is from well C. XRF is shown in solid line, and LIBS is shown in dots. XRF was measured every 2 inches and LIBS was measured every 1 foot. Most of LIBS data points lie on the XRF data.

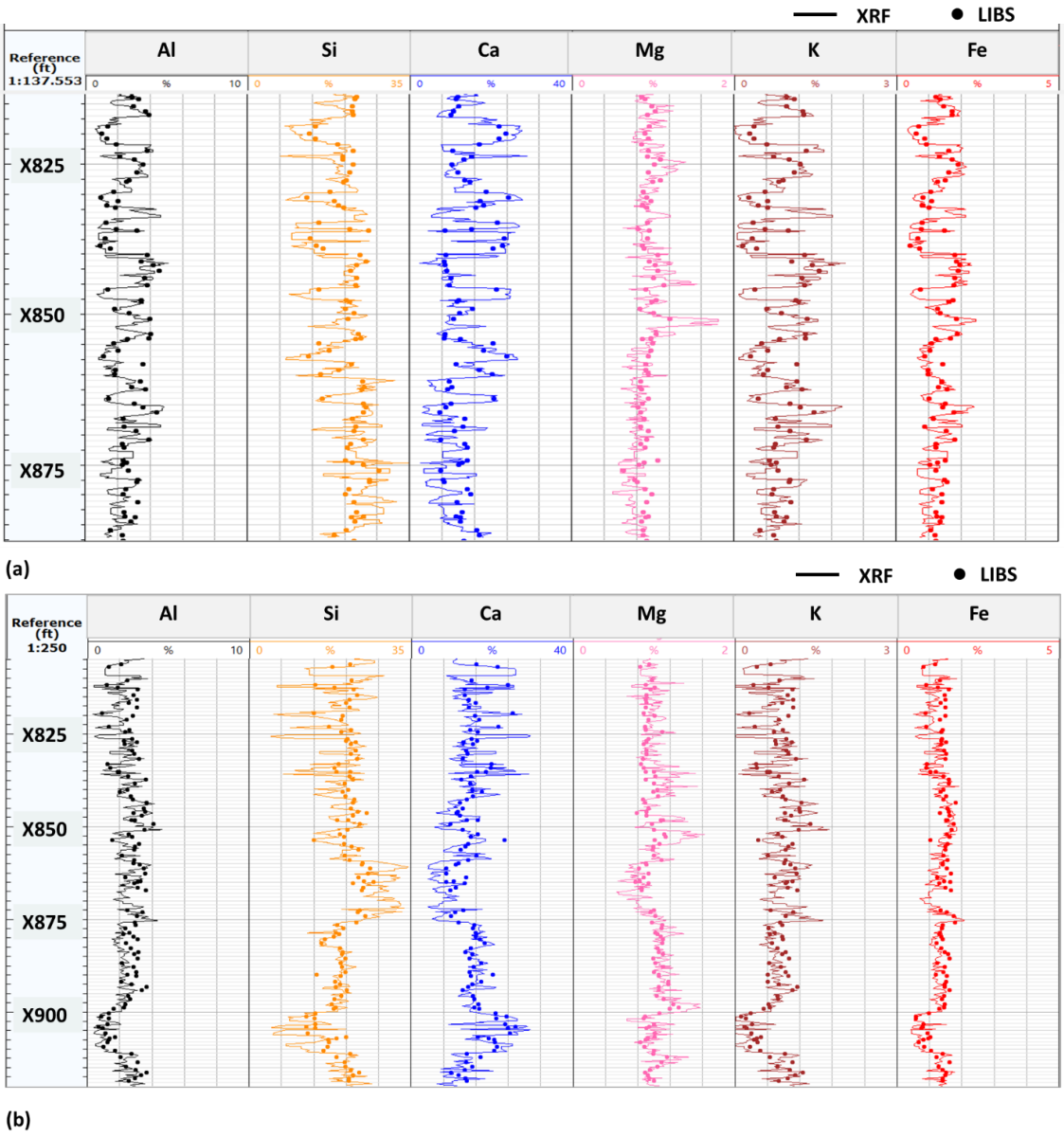

Figure 36: Elemental comparison between XRF and LIBS. (a) is from well B and (b) is from well C. The Continuous line indicates XRF data and dots indicate LIBS data. They agree well each other.

Appendix B: Mineralogy comparison between XRF and LIBS

Using our internal inversion software, elemental data can be converted into mineralogy. **Fig. 37** shows the mineralogy comparison inverted from XRF and LIBS on well G. Six minerals including quartz, calcite, dolomite, feldspar, clay, and siderite are shown. XRF-mineralogy is shown in solid

line and LIBS-mineralogy is shown in dots. Each track represents different minerals and they agree well each other.

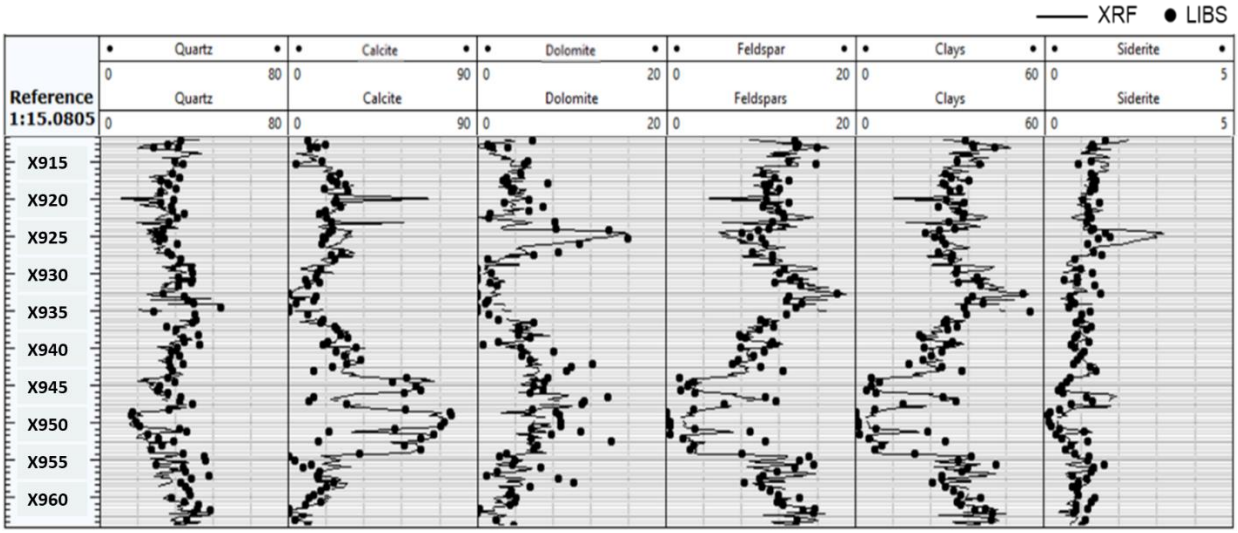

Figure 37: Mineralogy comparison between XRF-mineralogy and LIBS-mineralogy of well G. Elemental data acquired from either XRF or LIBS were inverted into mineralogy using internal inversion program. Solid line indicates XRF-mineralogy, and dots line indicate LIBS-mineralogy. Most of LIBS-mineralogy data points lie on the XRF-mineralogy data following the same trend.

Appendix C: Mineralogy comparison between XRF and FTIR

One to one cross plots between XRF-mineralogy and FTIR mineralogy were previously shown in **Fig. 21** for four wells: well B, C, D, and F. **Fig. 38** shows the mineralogy comparison on the continuous core sample from well D. Red line indicates XRF mineralogy and black dots indicate FTIR. X-axis shows the depth of core and y-axis shows the weight % of the mineral. In general, they agree well throughout the entire core.

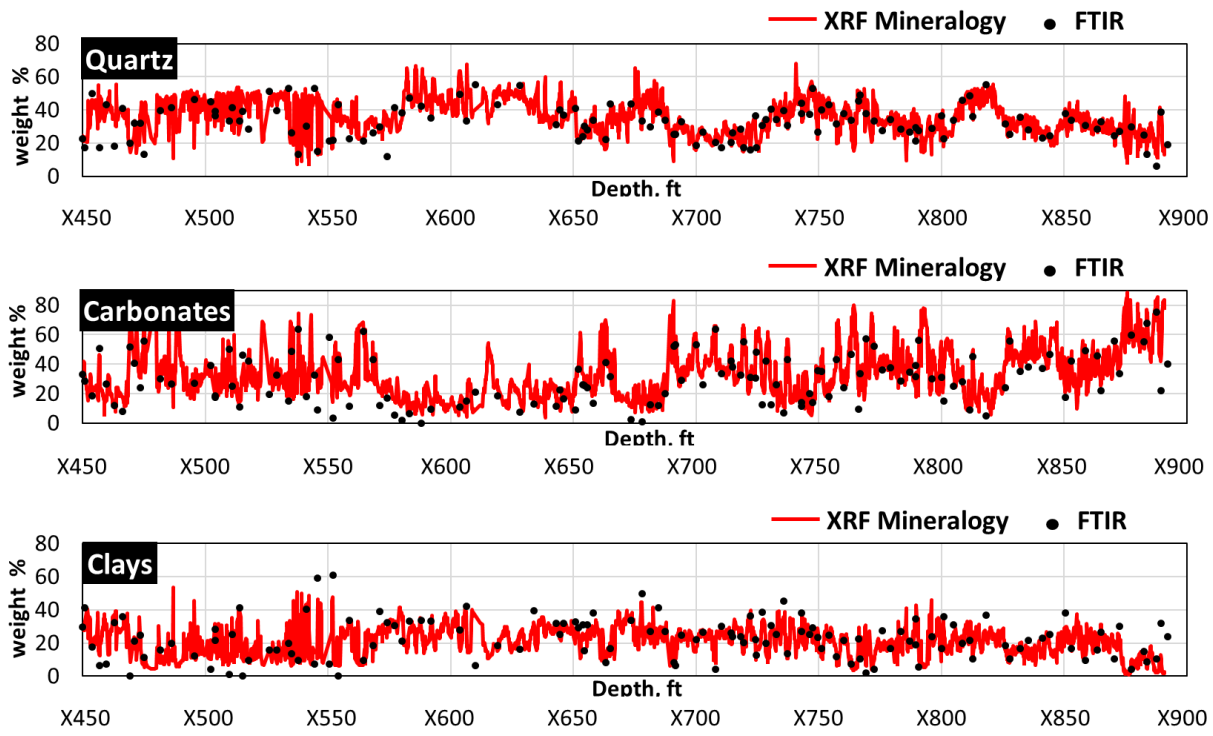

Figure 38: The mineralogy comparison between XRF-mineralogy and FTIR from well D. X-axis shows the depth of core and y-axis shows the weight % of the mineral. Red line indicates XRF mineralogy and black dots indicate FTIR mineralogy. They agree well each other throughout the entire core as most of FTIR data points are lying on XRF Mineralogy profile.

Appendix D: Mineralogy comparison between XRF and XRD

Fig. 39 shows the mineralogy comparison between XRF and XRD from well E. X-axis shows the depth of core and y-axis shows the weight % of the mineral. Red line indicates XRF-mineralogy and black dots indicate XRD from a service company. For quartz, XRD seems to overestimate compared to XRF-mineralogy. On the contrary, for clays, XRD seems to underestimate compared to XRF-mineralogy.

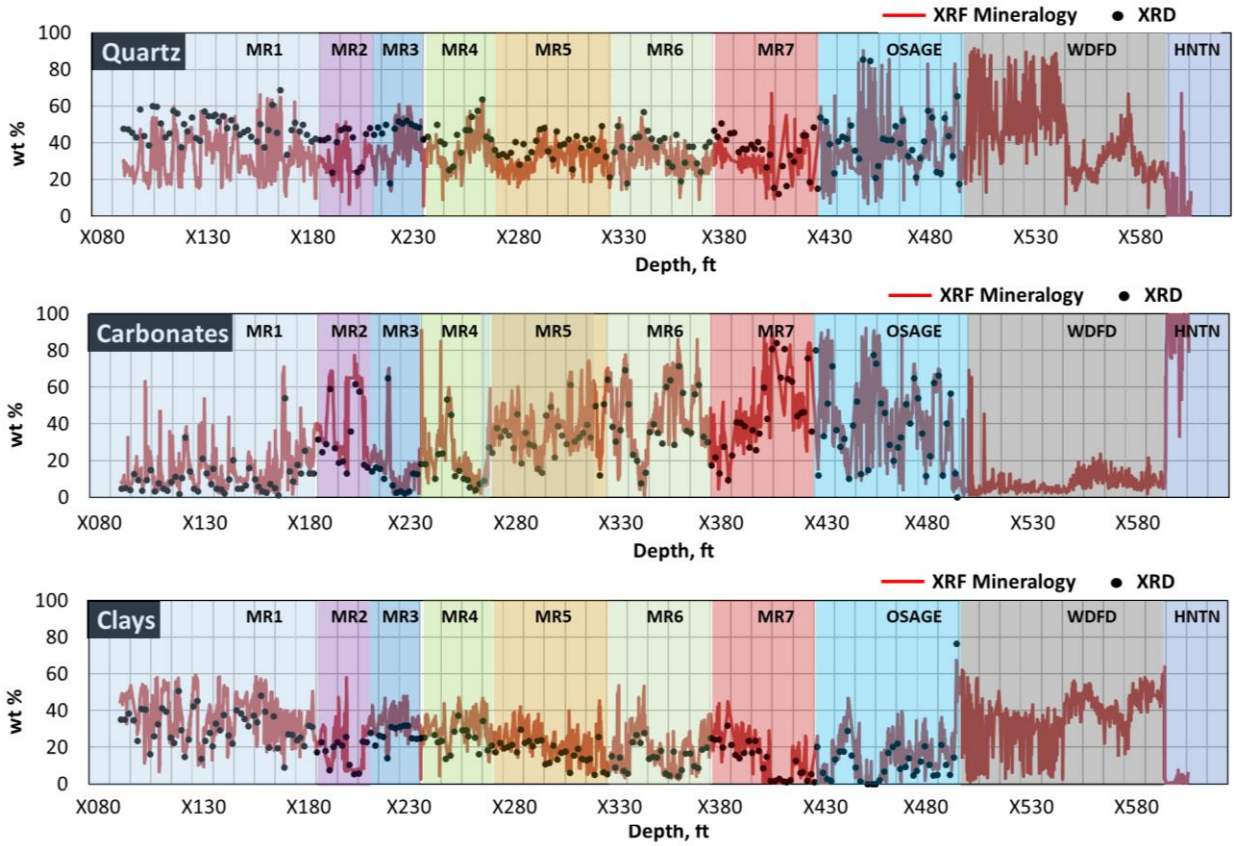

Figure 39: Mineralogy comparison between XRF and XRD from well E. X-axis shows the depth of core and y-axis shows the weight % of minerals. Red line indicates XRF mineralogy and black dots represent XRD data proved from a service company. For quartz, XRD seems to overestimate compared to XRF-mineralogy. On the contrary, for clays, XRD seems to underestimate compared to XRF-mineralogy.

Appendix E: TOC comparison between LIBS and LECO® measurements

LIBS can detect total carbon, both organic and inorganic carbon. Following the workflow depicted in **Fig. 17**, TOC concentration was acquired using LIBS measurements. **Fig. 40-a** shows the TOC comparison between LIBS and LECO® measurement on the continuous core from well D. This core contains Woodford section colored in grey. Half of the Woodford section in the red box shows that LECO® TOC overestimates compared to LIBS data. Considering the higher concentration of carbonates in the section (**Fig. 39**) it is thought that samples in the red box area need to be acidized

more to remove inorganic carbon from carbonates. **Fig. 40-b** shows the total carbon from LIBS in red and LECO® TOC in black dots, and black dots lie on the LIBS total carbon line. It suggests that LECO® TOC contains some amount of inorganic carbon concentration.

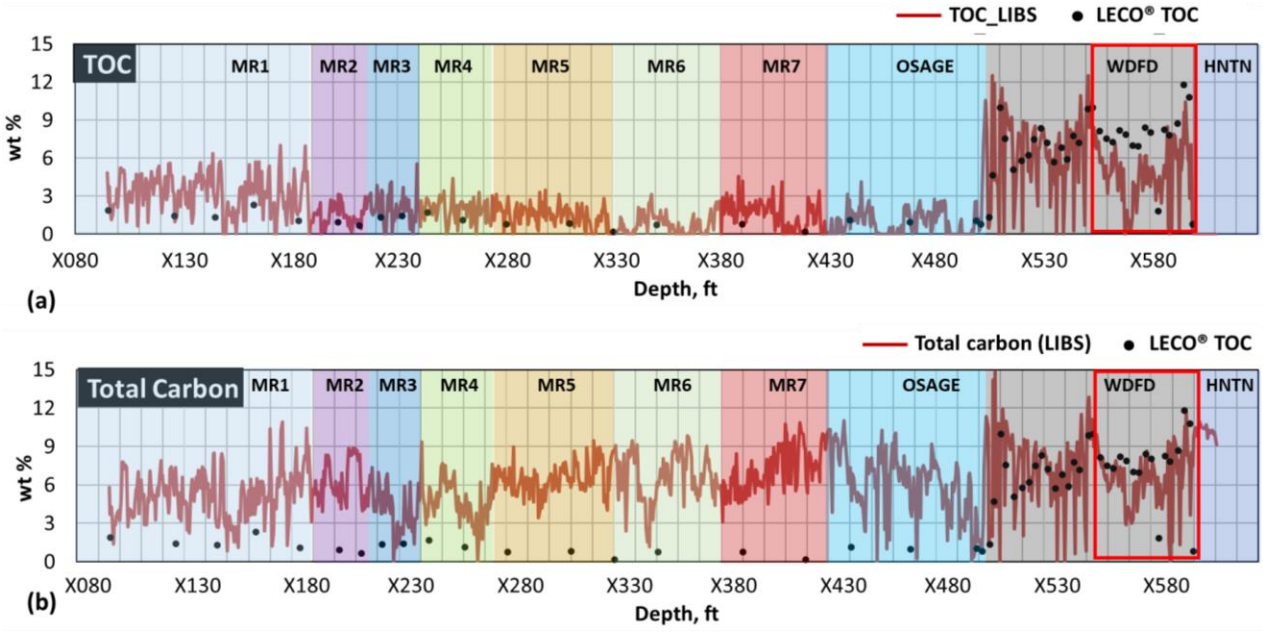

Figure 40: (a) TOC comparison between LIBS and LECO® TOC from well D. This core contains Woodford formation colored in grey. Half of the Woodford section in the red box shows that LECO® TOC overestimates TOC compared to LIBS data. Considering the higher concentration of carbonates in that section (Fig. 39) it is thought that samples in the red box area need to be acidized more to remove inorganic carbon. (b) Total carbon from LIBS is shown in red and LECO® TOC is shown in black dots. Black dots lie on the LIBS total carbon line in the red box area and it suggests that LECO® TOC may contain some amount of inorganic carbon.

Fig. 41 shows the Woodford section expanded from **Fig. 40**. Mo and V concentrations which are being used as an indication of redox conditions from XRF data are added on. **Fig. 40 (a)** shows TOC comparison including Mo (molybdenum) concentration in green. **Fig. 40 (b)** shows TOC comparison including V (vanadium) concentration. Mo and V concentrations are indicated on the right-hand side y-axis in weight %. Mo and V demonstrate the complicated interplay of multiple factors controlling bottom water circulation (Turner, 2016). They show distinctively high

concentration in the Woodford formation compared to Meramec. However, Mo remains low concentration on top of Woodford (orange shaded) and V does not show much of variation in WDFD_MID section (blue shaded).

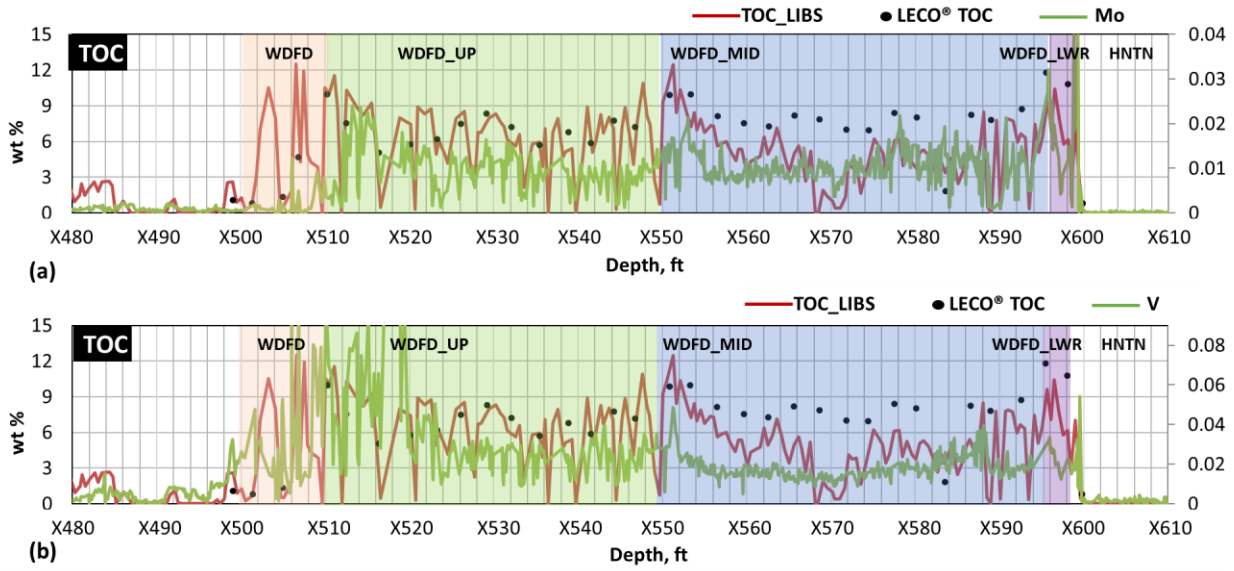

Figure 41: LIBS and LECO® TOC comparison for the Woodford formation which is expanded from Fig. 40 grey shaded area. Mo and V concentrations acquired from XRF are included and their scales are shown on the right-hand side y-axis. Mo and V show distinctively high concentration in Woodford formation compared to Meramec. However, Mo remains low concentration on top of Woodford (orange shaded) and V does not show much of variation in WDFD_MID section (blue shaded).

Appendix F: Inversion for mineralogy from elemental data

Most minerals found in rocks are mainly composed of eight elements: silicon, aluminum, calcium, magnesium, sodium, potassium, iron and sulfur. **Table. 4** shows the elemental concentrations for each mineral. Since we know the elemental concentration for each mineral, the total elemental concentration in the sample can be calculated based on the Equation 5.

$$C_{i,bulk}(wt\%) = \sum_{i=1} C_{min,bulk}\, C_{i,min} \qquad Eq.5$$

Where, *i* represents each element and *min* represents each mineral (Craddock et al., 2016).

Table 4: Elemental concentration of each mineral. This table is modified from Craddock et al., 2016.

Mineral	Elemental Composition, wt%							
	Si	Al	Ca	Mg	Na	K	Fe	S
Quartz	46.7							
K-feldspar	30.0	10.0	0.1		2.0	10.2	0.2	
Plagioclase	29.6	11.8	3.0		6.9			
Calcite			39.5	0.4				
Dolomite			21.3	12.9				
Illite	24.0	13.2	0.6	1.2	0.7	4.8	4.8	
Smectite	24.6	10.0	1.5	2.4	0.7	0.6	2.1	
Kaolinite	20.8	20.4	0.1	0.1	0.1	0.1	0.4	
Chlorite	14.0	9.6	0.7	4.8	0.1	0.4	20.8	
Pyrite							46.6	53.5

Fig. 42 shows the input and output data of our inversion software. Since many minerals share the same elements with similar concentrations and the number of inputs is smaller than the number of outputs, our inversion requires elemental data and the specification of three mineral ratios: 1) clay/feldspar; 2) chlorite/siderite and 3) smectite/kaolinite. Those mineral ratios are from FTIR mineralogy data.

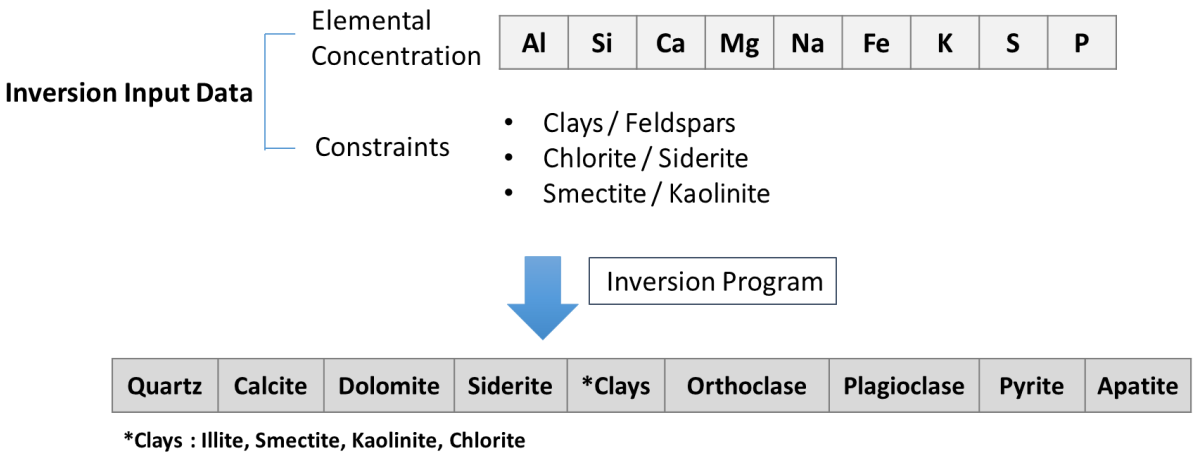

Figure 42: Input and output data of our inversion. It requires elemental data with three constraints. Our inversion provides 12 different minerals.

Appendix G: List of wells

Four wells discussed on this paper are from the Oklahoma Geological Survey core facility (OPIC).

The names of well are indicated in **Table 5**.

Table 5: Names of wells acquired from the Oklahoma Geological Survey core facility (OPIC).

Label	Well name
Well B	Shaffer
Well C	Rohling
Well G	Payne
Well H	Vanhorn